THE UNIVERSITY OF CHICAGO

CALIBRATING THE COSMIC DISTANCE SCALE IN THE MAGELLANIC CLOUDS WITH A SUB-PERCENT DETERMINATION OF THE BRIGHTNESS AT THE TIP OF THE RED GIANT BRANCH

A DISSERTATION SUBMITTED TO
THE FACULTY OF THE DIVISION OF THE PHYSICAL SCIENCES
IN CANDIDACY FOR THE DEGREE OF
DOCTOR OF PHILOSOPHY

DEPARTMENT OF ASTRONOMY AND ASTROPHYSICS

BY

TAYLOR J. HOYT

CHICAGO, ILLINOIS

AUGUST 2022

I am exceedingly grateful to so many important mentors, friends, and especially my family whose support has brought me to this moment.

In particular, I acknowledge,

My Ph.D. advisor Wendy Freedman for her empathetic leadership and for believing in me when I found it difficult to do so myself.

Hsiao-Wen Chen for eye-opening discussions that have helped me retain my optimism and grow from the rough patches I've hit while pursuing my PhD.

Mike Gladders for his much needed presence and understanding.

Laticia Rebeles for her friendship and willingness to listen.

Don Winget and Mike Montgomery for inspiring me to pursue astrophysics while a part of their brilliant undergraduate research program.

Peter Garnavich for the REU opportunity that set me on the path to come to Chicago and pursue research into the expansion rate.

Cecilia Lara for acknowledging and helping me learn to take pride in my scholarship.

So many people are looking for news on the go. If you really want to understand the world, you're not going to by consuming news in the form of bite-sized haikus. – Michele Norris

TABLE OF CONTENTS

LIST OF FIGURES

LIST OF TABLES

ACKNOWLEDGMENTS

I am indebted to Prof. Wendy L. Freedman for her invaluable support and tutelage throughout my graduate studies, as well as insightful comments on, and discussions regarding, this manuscript. Prof. Andrzej Udalski and the OGLE Collaboration are acknowledged for making publicly available the photometry from their revelatory survey. I thank Drs. Dorota and Jan Skowron for making publicly accessible their reddening maps of the MCs. I thank Drs. Jason Harris and Dennis Zaritsky for making publicly available their SFH maps of the LMC. I am thankful for the frequent, fundamental insights of Dr. Barry Madore. I am grateful to Prof. Hsiao-Wen Chen for heartening and encouraging discussions. I thank Dr. Rachael Beaton for stimulating discussions regarding the Clouds. I highlight the work of Dr. Mark Seibert who introduced the use of Voronoi tessellation to study resolved stellar populations, an approach that has since become commonplace in the literature. I thank Dr. In Sung Jang for helpful comments and clarifications. I am grateful to past and current members of the Carnegie Chicago Hubble Program from whom I have had the privilege to learn. I acknowledge Dr. Marios Karouzos for helpful comments and suggestions. I thank Clarke Esmerian for his helpful comments. I thank Dr. Brandon Hensley for inspiring a deep dive into the rich literature of observations acquired of the Clouds. This work has made use of data from the European Space Agency (ESA) mission *Gaia* (`https://www.cosmos.esa.int/gaia`), processed by the *Gaia* Data Processing and Analysis Consortium (DPAC, `https://www.cosmos.esa.int/web/gaia/dpac/consortium`). Funding for the DPAC has been provided by national institutions, in particular the institutions participating in the *Gaia* Multilateral Agreement.

ABSTRACT

The present-day expansion rate of the universe as constrained by Type Ia supernovae (SNe Ia) is directly tied to the zero point of the extragalactic distance scale, which is in turn set by the calibration of astrophysical distance indicators such as the Tip of the Red Giant Branch (TRGB). In this study, a new calibration of the TRGB luminosity is determined in the Magellanic Clouds (MCs). Composite TRGB measurements are constructed for the Small and Large MCs from individual regions in which the TRGB could be unambiguously identified. As a result, the highest accuracy measurement of the TRGB in the Clouds to date is determined. The I vs. $(V-I)$ relation of the TRGB is found to be consistent with a constant I magnitude over colors $1.45 < (V-I)_0 < 1.95$ mag, and a shallow, quadratic curvature is confirmed when including more metal-rich (up to $(V-I)_0 = 2.2$ mag) Tip stars into the fit. The new measurements are calibrated from apparent brightness to absolute luminosity with reddening maps from the OGLE-IV survey based on observations of the Red Clump (RC), and the Araucaria Project's latest high-accuracy geometric distances based on detached eclipsing binaries (DEBs). This study's TRGB measurements place novel constraints on the three-dimensional tilt of the LMC as well as the distance between the Small and Large Clouds. Both findings are in agreement with the independent, geometric constraints derived from the DEBs and establish a better than 0.02 mag cross-consistency (1% in distance) between the latest DEB measurements, RC reddening maps, and the TRGB measurements of this study.

CHAPTER 1

MAIN

1.1 Introduction

The Hubble Tension—a difference between direct measurements of the present day expansion rate of the universe (or Hubble constant, H_0) that do not rely on a cosmological model versus those that are inferred under the assumption of the standard cosmological constant and cold dark matter (ΛCDM) model of the universe—remains a pressing question and potentially a signal of new physics. Improving the accuracy of direct H_0 measurements is necessary to ascertain the nature of the Hubble Tension; that is, the question of its existence and, if confirmed, the determination of its size. The distance ladder approach is currently the most precise and accurate method for directly measuring H_0. Indeed, we have reached a 3-4% consensus between the Tip of the Red Giant Branch (TRGB) and Cepheid calibrations of the SN Ia distance scale,[45, 28, 12, 46] with 1-2% disagreements intensely debated.[74, 43, 13, 29, 56, 1, 11]

The TRGB is observed in the empirical Hertzsprung-Russell (H-R), or color-magnitude, diagram (CMD), which encodes information about the luminosities (magnitudes) and temperatures (colors) of astronomical objects. A low-mass star that is increasing in luminosity, or ascending the H-R diagram, along the red giant branch will undergo a seconds-long thermonuclear runaway event after its once-inert He core reaches temperatures to fuse He. This Helium Flash initiates a rapid evolution off of the RGB and toward evolutionary stages that are bluer and up to two orders of magnitude fainter, i.e., the Horizontal Branch or the Red Clump (RC). This rapid migration in luminosity-temperature (or magnitude-color) space leaves behind a sharp discontinuity in the observed counts of stars at the "Tip" of the RGB. And due to the identical levels of core degeneracy reached by stars below masses $M \sim 1.8 M_\odot$ at the time of the Helium Flash, their luminosities at the TRGB are almost perfectly invari-

ant, particularly when observed through the Johnson-Cousins I-band ($\lambda_{eff} \sim 800$ nm).

A recent point of contention in the ongoing distance scale debate has centered on calibration of the TRGB in the Magellanic Clouds (MCs). The MC system is perfectly suited for absolute calibration of the TRGB distance scale. To the LMC and SMC, respectively, 1% and 2% distances have been geometrically derived from late-type detached eclipsing binaries (DEBs) for which a relation between their surface brightnesses and infrared (IR) colors has been constrained to better than 0.02 mag in total dispersion (or 1% in distance). [19, 41, 20, 21, 42, 22] Furthermore, compared to other Milky Way satellites, the Clouds contain relative to their integrated masses a uniquely high proportion of stars that are old and metal-poor,[37] which are the requisite conditions for the TRGB to manifest at a standard surface luminosity.[51]

So far, debate in the literature over the MC-based calibration of the TRGB has focused entirely on the effects of dust attentuation along TRGB star sightlines.[27, 17, 12, 74, 18, 13, 55, 36, 56] But even after removing the reddening issue from the equation, there is still an 8% disagreement (despite 1-2% quoted uncertainties) over the mean *apparent* brightness of the TRGB as observed in the LMC—a glaring problem that has yet to be satisfactorily addressed.

In this dissertation, the sources of this discrepancy are rectified with a novel sample selection methodology aimed at filtering out imprecise TRGB signals. It is found that some earlier studies of the LMC TRGB were biased by these anomalously faint and imprecise TRGB features. By selecting only regions of the LMC with a well-defined TRGB that are also free of evidence for significant recent star formation, a sub-percent determination of the TRGB magnitude in the Clouds—the most precise and accurate to date—is attained.

1.2 Data

The OGLE collaboration has been monitoring the MCs since the late 1990s [62, 63, 64, 66, 67] and with each iteration our understanding of them has advanced considerably. The publicly available OGLE-III [65] photometric maps (recalibrated using OGLE-IV observations of the bulge).[60] are adopted for the present analysis. The photometry is trimmed to include only sources on the upper-RGB ($I < 17$ mag, $(V - I) > 0.5$ mag).

Duplicate sources defined as within 0.2" of another source (about a factor of five smaller than the minimum seeing at the Warsaw telescope) in the OGLE maps are merged via weighted average of their respective mean fluxes, using the number of good observations underlying each mean flux as the weights. All duplicate candidates are located on the survey's chip and field boundaries. Also, magnitude differences between duplicate candidates are far below the standard deviation of each source's photometry. Both points indicate that all candidates are true duplicates and not fluke matches.

High amplitude long-period variables (those classified as Miras or semi-regular variables) in either Cloud[57, 58] are masked.

For the TRGB calibration in the LMC, both the OGLE-Shallow[68] and OGLE-III photometric maps (`http://ogle.astrouw.edu.pl/cont/4_main/map/map.html`) are considered because one or the other has been used in various prior studies of the TRGB in the LMC. Note, though, the primary OGLE-III catalog was adopted for the final measurements given its much higher photometric precision.

1.2.1 Gaia Proper Motion Cleaning

Foreground sources are removed from the photometric catalogs using Gaia[14] EDR3[15] proper motions.[32, 9, 61]

All bright Gaia EDR3 sources within 5.5 deg of the LMC center ($\alpha = 80.9^d, \delta = -69.75^d$) are queried in order to select upper RGB stars contained in the OGLE-III footprint. The

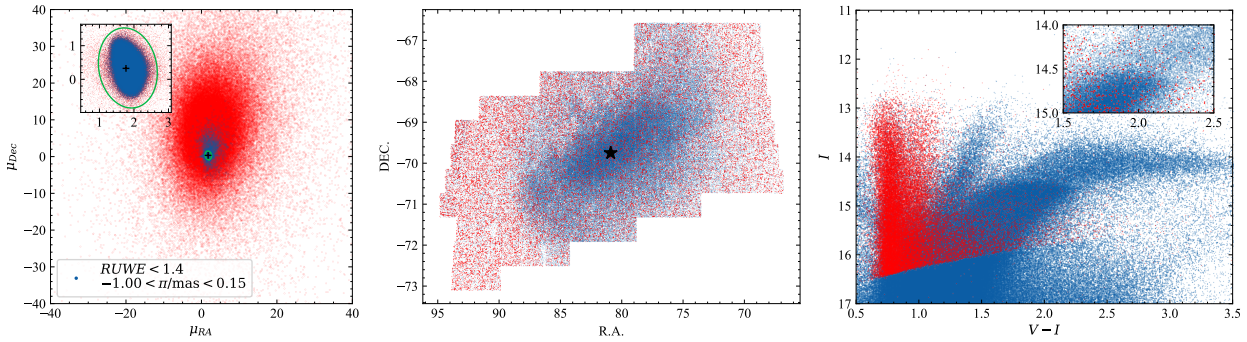

Figure 1.1: **Cleaning Foreground Sources with Gaia EDR3 Proper Motions. a.** Distribution of EDR3 proper motions for the LMC. Sources with small parallaxes (blue points) are used to define an elliptical proper-motion profile (green ellipse). Sources outside the parallax cut are also plotted (red points). The LMC proper motion determined by the Gaia Collaboration[16] is plotted for reference (black plus sign). All sources outside the green profile are excluded as foreground. To avoid unintentionally clipping real LMC sources, only sources with $RUWE < 1.4$ are considered for cleaning. **b.** Distribution of OGLE-III sources on the sky. Sources identified as foreground (red dots) are plotted over LMC member stars (blue dots). **c.** Same but in color-magnitude space. A zoomed view of the TRGB is shown in the inset.

SQL query was,

```
SELECT edr3.source_id, edr3.ra, edr3.dec,
edr3.parallax, edr3.parallax_error,
edr3.pm, edr3.pmra, edr3.pmra_error,
edr3.pmdec, edr3.pmdec_error,
edr3.ruwe, edr3.phot_g_mean_mag,
edr3.phot_rp_mean_mag, edr3.bp_rp,
FROM gaiaedr3.gaia_source as edr3
WHERE 1=CONTAINS(POINT('ICRS',edr3.ra,edr3.dec),
CIRCLE('ICRS',80.9,-69.75,5.5))
AND edr3.phot_g_mean_mag < 17
```

The same query is done for the SMC but for all sources within 3 deg of the its center ($\alpha = 12.5^d, \delta = -73.0^d$), and a limit $G < 17.5$ mag. This returned 570119 and 200718 sources

for the LMC and SMC, respectively. To ensure that only sources with well-measured proper motions are considered for removal as foreground contaminants, a cut on $RUWE < 1.4$ is made.[31]

To isolate the underlying distribution of MC proper motions, an initial cut of $-1 < \pi < 0.15$ mas is made (Figure 1.1a). Note this does *not* define the final PM selection. It is only used temporarily to filter out most of the foreground sources and enable determination of the 2D proper motion profiles. An extreme overdensity of sources is found near the expected values for the proper motions for each Cloud[16] (black crosshair in Figure 1.1a) and is used to define an elliptical profile for the proper motion distribution (green curve in Figure 1.1a). The sources identified as foreground exhibit a uniform distribution in on-sky coordinates (Figure 1.1b) and an expected distribution in color-magnitude space (Figure 1.1c). PM cleaning removes $\sim 35,000$ foreground sources from the LMC OGLE-III catalog, and $\sim 15,000$ from the SMC OGLE-III catalog.

1.2.2 Reddening Corrections

Adopted for the reddening corrections is a recent map released by the OGLE collaboration that used the observed colors of RC stars to measure line of sight reddening values across the entirety of each MC, reaching resolutions of $1.7' \times 1.7'$ (approximately 20 pc) in their inner regions.[55] In Figure 1.2, this new OGLE-IV reddening map is shown along with the earlier OGLE-III survey's footprint. The large area covered by the OGLE-IV survey enabled a new, direct calibration of the RC intrinsic color using the Schlafly and Finkbeiner (SF11) [53] re-normalization of the Schlegel et al. (SFD98)[54] maps in the outer regions of the MCs where the foreground maps become reliable, a concept identical to an earlier work on early-type eclipsing binaries.[39] Importantly, this places the de-reddened TRGB measurements of this study on the exact same SFD98/SF11 Galactic reddening zero point as the SN Host sample that constitutes the TRGB-SN H_0.

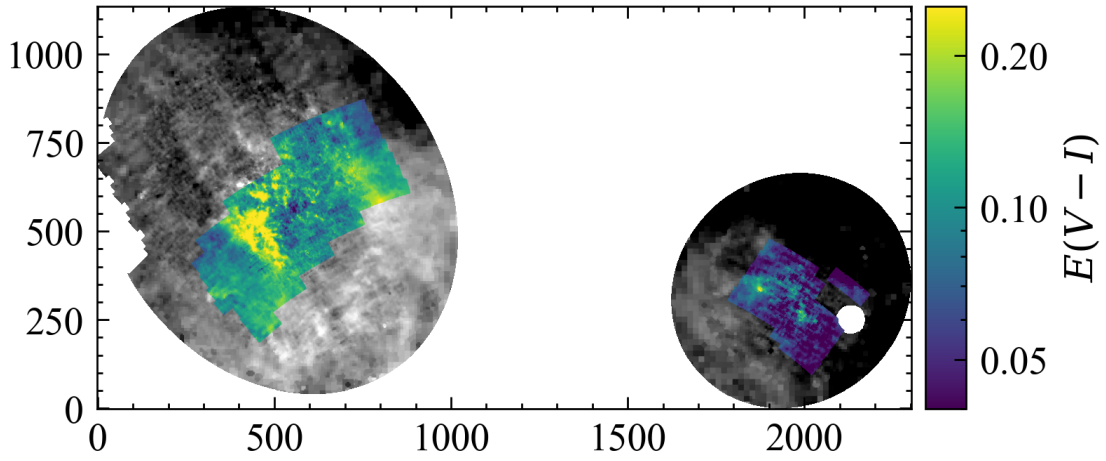

Figure 1.2: The OGLE-IV [55] Red Clump (RC) $E(V-I)$ reddening map of the Magellanic Clouds plotted on the map's native pixel grid (a Hammer projection). Regions also covered by the OGLE-III survey are hued to a Viridis color map, while the rest of the map is in grayscale. Note the log stretch.

The RC has been used numerous times to quantify dust attenuation along MC sight lines [24, 39, 4, 18, 55] and has produced consistent results in a relative sense. However, there was some debate over the calibration of the RC's intrinsic color as observed in the MCs.[18, 55, 36] The calibration of the RC intrinsic color is fundamentally tied to an eventual zero point calibration of the TRGB that uses RC-determined reddening corrections (for reference, bluer RC intrinsic color calibrations result in larger measured reddening values). The reader is referred to Section 5 of the OGLE-IV reddening paper[55] for a discussion of prior determinations of the RC intrinsic color and why their result is the state-of-the-art, likely accurate, and preferred for this analysis.

To summarize, the OGLE-IV RC map is comprehensive, fully empirical, and most applicable to the OGLE photometry adopted here. Each calibration step that is required to use the RC as a standard crayon was undertaken using only homogeneous measurements made directly in each Cloud (rather than invoking theoretical predictions or external photometry). These steps include: (1) a direct calibration of the RC intrinsic color made in the outer regions of each MC via SFD98/SF11 foreground maps, (2) empirical determination of

the metallicity gradients in each Cloud using recent APOGEE abundance measurements,[37] and (3) an empirical calibration of the RC color-metallicity relation using homogeneous photometry of clusters in the MCs. For these many reasons, the OGLE-IV reddening maps are optimal for this OGLE-based calibration of the TRGB. This view is shared in the literature, e.g., Soltis et al. [56] state that the new OGLE-IV maps are a "significant improvement" over a frequently-used, earlier RC reddening map based on OGLE-III photometry and a theoretical calibration of the RC intrinsic color.[24] Furthermore, the OGLE-IV reddening study found agreement with Nataf et al. [36] on the metallicity dependence of the intrinsic RC color.

Throughout this article, the following reddening law coefficients are adopted: $E(V-I) = 1.4E(B-V)$, and $A_I = 1.219E(V-I)$. The former is computed directly from the SF11 Landolt coefficients for $R_V = 3.1$, while the latter is computed by taking the Fitzpatrick [10] curve (built from the spline points provided in their Table 3) and convolving it with the OGLE-IV flux transmission curve (`http://ogle.astrouw.edu.pl/main/OGLEIV/mosaic.html`).[1] Dereddened magnitudes and colors are always indicated with naught subscripts.

1.2.3 Construction of LMC Star-formation History Maps

To estimate the contribution from intermediate-aged (200 Myr$< t <$ 2 Gyr) and young ($t <$ 200 Myr) populations relative to the LMC's old ($t >$ 4 Gyr) stellar population, the following quantities are calculated from the star formation history (SFH) maps of Harris

1. The difference between this exact calculation of the selective to total absorption and the Landolt values provided in SF11 is 0.19%, and thus used solely for the sake of completeness, having no measurable effect on the absolute photometry used here.

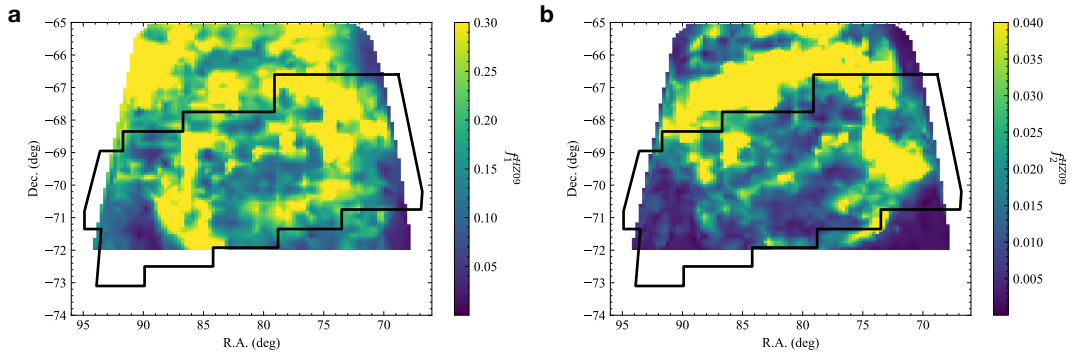

Figure 1.3: **Maps of Intermediate-age and Young Stellar Populations in the LMC.** The Harris & Zaritsky (HZ09) SFR maps are integrated into mass bins that represent intermediate-age (panel a) and young (panel b) stellar populations (integrals defined in Equation 1.2). A black outline indicates the coverage of the OGLE-III photometric maps adopted for this study. Known star-forming structures such as the LMC's Northern spiral arm and the 30 Dor star-forming region ($\alpha \simeq 85°, \delta \simeq -69°$) are prominent.

and Zaritsky [23].

$$f_1^{HZ09} = \frac{\int_{t>200Myr}^{t<2Gyr} SFH_{HZ09}(t)dt}{\int_{t>4Gyr} SFH_{HZ09}(t)dt} \tag{1.1}$$

$$f_2^{HZ09} = \frac{\int^{t<200Myr} SFH_{HZ09}(t)dt}{\int_{t>4Gyr} SFH_{HZ09}(t)dt} \tag{1.2}$$

The f_1 and f_2 quantities are then normalized, i.e.,

$$r_{1/2}^{HZ09} = \frac{f_{1/2}^{HZ09}}{< f_{1/2}^{HZ09} >} \tag{1.3}$$

and assigned individually to sources in the OGLE photometric catalog nearest each pixel of the SFH maps. The normalizing values $< f_1 >$ and $< f_2 >$ are 0.107 and 0.018, implying, on average, a 9% and 2% contribution to the inner LMC's total mass from intermediate-aged and young stellar populations, respectively.

Two-dimensional maps of each quantity are shown in Figure 1.3, which reveal known star-forming structures of the LMC: 30 Doradus, the arm that extends from the W to the

N, and the star-forming bar.

1.2.4 LMC Geometric Corrections

In order to accurately calibrate the zero point of the TRGB in the LMC, the effect its on-sky orientation has on the observed distances to stars must be modeled and removed. To do so, the predicted line-of-sight distance to a test particle embedded in the infinitely thin LMC plane is computed via,[73]

$$
\begin{aligned}
& r(\alpha, \delta; \{\theta, i\}) = \\
& - R_{\mathrm{LMC}} \cos i \{ \cos\delta \sin(\alpha - \alpha_0) \sin\theta \sin(i) \\
& + [\sin\delta \cos\delta_0 - \cos\delta \sin\delta_0 \cos(\alpha - \alpha_0)] \cos(\theta) \sin(i) \\
& + \cos(i)(\cos\delta \cos\delta_0 \cos(\alpha - \alpha_0) + \sin\delta \sin\delta_0) \}^{-1}
\end{aligned}
\tag{1.4}
$$

Note that the angle θ in the above equation is measured North of West, while the Astronomical convention is East of North, defined as $\Theta = \theta - 90^\circ$, following the nomenclature of van der Marel et al. [72].

Three thin plane geometries are considered for computing the line-of-sight distance corrections: 1) that determined from the Araucaria Project's 20 DEBs ($\Theta = 132^\circ$, $i = 25^\circ$), 2) that determined from a sample of 30000 RR Lyrae observed by the VMC (VISTA Magellanic Clouds) Survey ($\Theta = 167^\circ$, $i = 22^\circ$)[6], and 3) that determined in this study using the TRGB ($\Theta = 153^\circ$, $i = 27^\circ$; see subsection 1.4.7). These three sets of parameters comfortably cover the typical ranges of values for the LMC's on-sky geometry[73, 72, 38] and will therefore successfully probe the full effect that adoption of a geometric model has on the final TRGB calibration. The minimal effect that different geometric model assumptions have on the final TRGB measurement is discussed in chapter 2.

1.3 TRGB Measurement Methodology

To measure the TRGB magnitude, a methodology used by the Carnegie Chicago Hubble Program (CCHP) is adopted.[25] From a color-magnitude diagram (CMD), the RGB luminosity function (RGB LF) is isolated with a color-magnitude selection. The boundaries of the selection used in the final measurements were determined by squeezing each edge separately until the TRGB magnitude measured from the calibration sample no longer changed. By contrast, the color selection for the field-by-field TRGB measurements included all upper RGB stars to ensure a maximally populated RGB LF.

For the MC measurements, the RGB LF is binned at 0.002 mag intervals then smoothed via Gaussian-weighted Local Regression (GLOESS).[40, 34] To produce the edge detector response (EDR) from which the location of the TRGB is measured, the discrete first derivative of the smoothed RGB LF is weighted by the Poisson Signal-to-noise contributing to each bin,[33] i.e.,

$$w(i) = \frac{N_{i+1} - N_{i-1}}{\sqrt{N_{i+1} + N_{i-1}}} \tag{1.5}$$

The peak of the EDR then signals the measured location of the TRGB magnitude. When estimable, uncertainties for each TRGB measurement presented in this study are determined via bootstrapping the RGB LF and remeasuring the TRGB.

1.4 Measuring the TRGB in the LMC

As mentioned, there is in the recent literature a statistically significant disagreement regarding the apparent mean TRGB magnitude as measured in the LMC. The most important factor behind this discrepancy is sample selection. That is, which RGB stars in the Magellanic Clouds and their coincident sightlines should be used to calibrate the extragalactic distance scale?

To answer this question, we must consider that the LMC contains complex star-forming

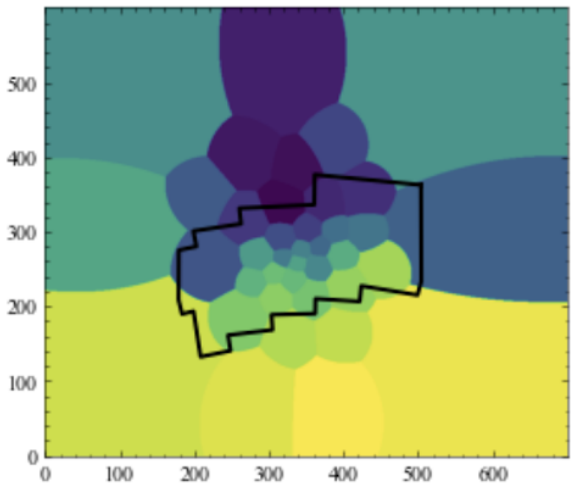

Figure 1.4: Voronoi tessellation map used to divide the LMC into spatial bins each with a constant number of RGB stars. The Viridis color mapping is discrete from 1 (dark/purple) to 39 (light/yellow). The footprint of the OGLE-III survey is shown (black outline). The 25 fields used in this study are contained within that footprint.

structures as was highlighted in the photometric SFH maps (Figure 1.3). Additionally, the TRGB's underlying physical mechanism (the Helium Flash event) only occurs at a cosntant luminosity in low-mass ($\lesssim 1.5\ M_{\odot}$) stars. As a result, the assumption that a handful of sub-fields situated in star-forming regions of the LMC can be an accurate representation of the TRGB luminosity (as has been done in most recent studies[27, 17, 74, 56]) will be prone to systematic error. On the other hand, using all of the available photometry of the LMC for one composite TRGB measurement and relying on the central limit theorem[12, 13] has the advantage of being more resilient to systematic biases in the calibration sample, but ultimately limits the precision of the TRGB measurement. In this study, a "best of both worlds" approach is taken. By considering the entirety of the publicly available photometric maps of the LMC and using a more sophisticated binning procedure than the equal-area bins of previous studies, the most precise and accurate determination of the LMC's TRGB magnitude is determined.

1.4.1 Dividing the LMC into Spatial Bins

In order to investigate the LMC TRGB as a function of location in the galaxy, the photometry was divided into 25 spatial bins that trace the isodensity contours of RGB stars and keep constant the signal-to-noise of the TRGB feature in each bin. These fields were constructed in a prior study of the LMC which divided the extended LMC disk into 39 bins of equal RGB star counts (Figure 1.4.[26] This requirement to first order normalizes the signal-to-noise of the TRGB feature observed in each bin.

The bin definitions were computed using Voronoi tessellation.[3] The algorithm starts with one "pixel," in this case the center of a rectangular bin of RGB stars on the sky, and continues to accrete the nearest pixels until all bins contain approximately a constant number of RGB stars. 25 of these Voronoi bins overlap with the OGLE-III photometry that was adopted for this study (see Figure 1.4). Central (source-density-weighted) positions for each bin are listed in Table 1.1 along with each bin's angular area on the sky. In addition, the median stellar content quantities r_1 and r_2, as well as the median OGLE-IV and SFD98 foreground reddening values for each spatial bin are also tabulated in Table 1.1.

Two tiers of cuts are then used to isolate the standard candle TRGB feature from the sloshy distribution of gas, dust, and star formation in the LMC.

1.4.2 First Set of LMC Selection Cuts

A TRGB magnitude was determined for each field using the corrected OGLE-III photometry. An inclusive color-magnitude selection is used to avoid introducing variations in RGB number statistics across bins. Bootstrapping is performed on the RGB LF within each spatial bin and the TRGB is redetected for 10000 realizations. The bootstrapped intervals and TRGB values are tabulated in Table 1.2.

As shown in Figure 1.5, 10 fields are cut via a clear delineation in the distribution of measured TRGB magnitude m_T and the corresponding 90% confidence interval as deter-

Field	R.A. (deg)	Dec. (deg)	Area (deg^2)	r_1^{HZ09} [a]	r_2^{HZ09} [a]	$E(B-V)^b$ (mag)	$E(B-V)^c$ (mag)
19	78.78	-70.10	0.9	1.02	0.56	0.070	0.287
11	90.01	-69.79	5.1	0.12	0.89	0.070	0.089
33	71.68	-69.88	3.0	0.68	2.13	0.104	0.132
32	75.58	-70.65	1.6	1.09	1.37	0.069	0.138
13	69.57	-68.27	3.4	0.32	0.89	0.064	0.073
29	79.58	-71.18	1.3	0.62	0.47	0.070	0.156
18	80.38	-69.50	0.4	0.31	1.25	0.050	0.924
27	81.53	-70.58	0.7	0.95	0.43	0.069	0.212
28	83.52	-70.29	0.5	0.77	0.96	0.072	0.409
5	77.79	-67.78	1.8	1.14	0.68	0.076	0.292
17	82.41	-69.78	0.4	0.37	1.34	0.058	0.363
25	76.14	-69.60	1.1	1.18	0.72	0.075	0.198
23	80.99	-69.98	0.3	0.37	1.51	0.071	0.518
6	74.54	-67.39	2.6	1.73	2.01	0.065	0.185
14	78.54	-69.34	0.5	0.48	1.32	0.077	0.828
30	87.53	-71.65	3.4	0.60	0.42	0.096	0.094
31	83.68	-71.31	1.2	0.83	0.77	0.086	0.262
26	86.24	-70.63	1.1	1.95	0.97	0.126	0.449
22	85.10	-69.70	1.3	1.48	0.94	0.161	1.329
15	76.94	-68.76	0.9	1.58	1.53	0.073	0.514
8	79.67	-68.79	0.9	1.36	0.59	0.081	0.571
7	85.72	-68.52	1.7	1.62	1.65	0.104	0.335
10	82.43	-69.05	1.0	1.34	0.95	0.082	0.509
16	73.94	-68.70	1.9	3.24	2.45	0.090	0.322
1	82.19	-68.10	0.9	0.88	0.90	0.101	0.520

Table 1.1: **Summary of the 25 LMC Voronoi Fields**. The bin spatial boundaries were defined in a prior study[26] to sample equal numbers of RGB stars. Of the 39 bins defined in that original wide-area study, 25 overlap with the full OGLE-III photometric maps adopted for this study's calibration. This table is sorted according to the width (90% CI) of bootstrapped TRGB realizations for each field (see subsection 1.4.2). Horizontal lines indicate the boundaries of each selection cut made to construct the calibration sample to match the order of Table 1.2 (see subsection 1.4.2 and 1.4.3).

[a] Star formation statistic. See Equation 1.2, 1.3.

[b] Median value from the OGLE-IV reddening map.[55]

[c] Median value from the SF11[53] recalibration of the SFD98[54] Galactic reddening map. These values are known to overestimate the foreground reddening in the inner regions of the LMC, due to contamination from LMC member stars.

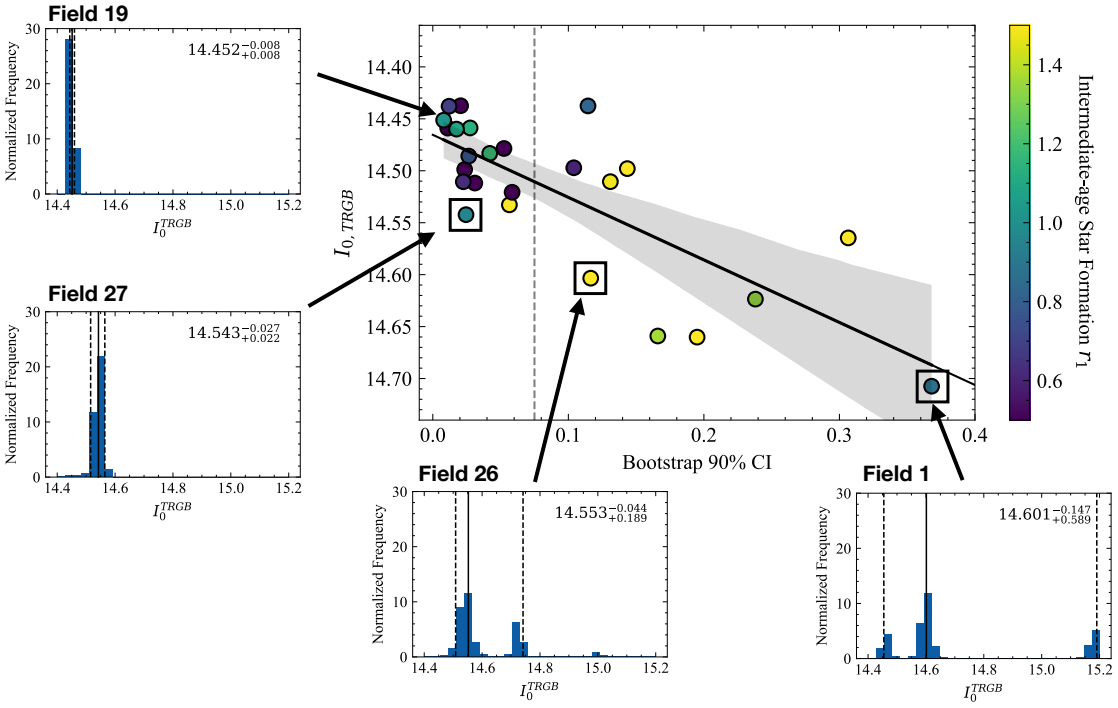

Figure 1.5: **Step One of the Sample Selection Procedure: Intra-field boostrapping results.** The likeliest TRGB magnitude $I_{0,TRGB}$ is plotted as a function of half the 90% confidence interval for each bootstrapped realization. A vertical dashed line indicates the first of two cuts used to clean the sample for optimal TRGB calibration accuracy. Four example distributions are shown. Large intervals are indicative of multimodal edge features spanning in some cases 0.8 mag in central value. Bin sizes are 0.01 mag for all histograms. NOTE: The values of $I_{0,TRGB}$ shown here were determined with a wider color selection than the composite LMC measurements (Figure 1.8) and cannot be directly compared to those values.

mined from the bootstrapping experiments. The fields with broader distributions in their bootstrapped values of m_{TRGB} are strongly ($p < 0.001$) found to exhibit fainter values of m_{TRGB} (black line and gray band in Figure 1.5). That is, fields with more imprecise TRGB features are also systematically biased to fainter mean TRGB magnitudes. This is consistent with the definition of the *tip* of the RGB being the brightest luminosity attainable by an RGB star. That is, any false edges that contribute noise to the CMD will also be necessarily fainter than the true TRGB magnitude (as visualized in Figure 1.5).

In Figure 1.5, the points are colored according to the r_1^{HZ09} parameter which was defined to trace intermediate-age stellar content and normalized to its average value across all fields. That is, fields with values $r_1 > 1$ have a population size of intermediate-age stars above the average. These fields are also predominantly located outside the adopted cut, suggesting the increased scatter in likely TRGB magnitudes in that region is related to population mixing or related effects.

1.4.3 Second Set of LMC Selection Cuts

Second, the structure of the EDRs are examined in order to isolate the fields of the LMC which exhibit a single clear discontinuity in the counts of RGB stars (Figure 1.6). In contrast to the first set of cuts, there is not a clear distinction in r_1 between the single- and multi-peaked fields at this stage. Either the population mixing that may be causing the multi-modal structure here is not captured by the adopted SFH maps, or something more subtle like variations in the reddening law are introducing discrepant, competing signals for the dereddened TRGB. In either case, by definition of the *Tip* of the RGB it is well-motivated physically to prefer the brightest signal as the true TRGB. The data independently support this reasoning as the only singularly-peaked EDRs cluster at a TRGB magnitude of $I_0 = 14.44$ mag. This cut removes another 10 fields from consideration, leaving 5 out of 25 initial bins to be used in the final calibration.

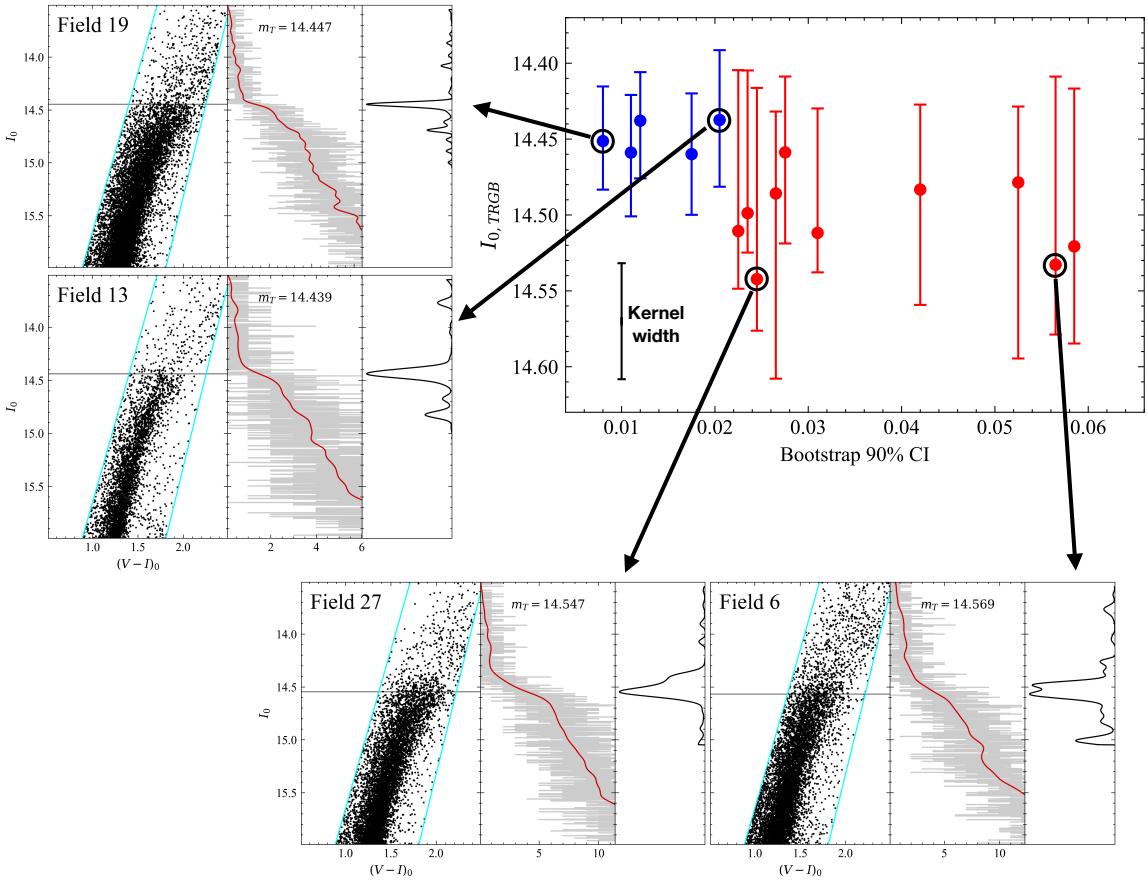

Figure 1.6: **Step Two of the Sample Selection Procedure: Shape of the EDR.** The peak TRGB magnitude of the EDR $I_{0,TRGB}$ is plotted as a function of half the 90% confidence interval for each subsampled realization (same as previous figure) with the error bars reflecting the 68% interval of the EDR. For four example fields the CMDs, RGB LFs, and EDRs are shown. The five fields with narrow, singularly-peaked EDRs (blue points) are adopted for the calibration. The width of the kernel used to smooth the RGB LF in each field is also shown (black capped line).

In Figure 1.6, example TRGB measurements are shown which highlight the nature of the second set of cuts. In recent studies of the TRGB in the LMC, blurred, multimodal Tip features such as those seen in Fields 6 and 27 led to measurable biases. Those studies reduced each field's TRGB feature into a single modal value with a symmetric standard error, as a result ignoring the long-tailed and multimodal nature of the EDRs seen in fields like the red ones shown here. In this study, that ambiguity is circumvented entirely by only retaining singularly-peaked EDRs (e.g., fields 19 and 13 shown here).

1.4.4 Additional Validation of Selection Cuts

The two quantitative metrics are independently in exact agreement that these five fields adopted for calibration are the "best" and form a distinct set of precise, unambiguous TRGB detections (seen in Figure 1.6). Importantly, the five fields are also distributed across the face of the LMC, extending from the Easternmost to the Westernmost edges of the survey footprint, decreasing the possibility of a spatial sampling bias.

Furthermore, in Figure 1.7 the spatial positions of various astrophysical tracers of recent star formation are plotted on top of the OGLE-IV reddening map, with the red fields corresponding to those cut in the first set of selection cuts, and orange fields those cut in the second set of cuts. The young bar as traced by the DEBs and Cepheids correlates very well with the orange fields in that same region. 30 Doradus and the Northern arm are traced well by the supergiant shells which also correlate well with the red fields.

1.4.5 TRGB Measurement

The spatially-resolved analysis has revealed that a pair of data-driven and astrophysically-motivated selection cuts significantly improve the accuracy of the TRGB calibration. Of the initial 25 spatial bins, five remain in the nominal calibration sample (blue regions in Figure 1.8a). This somewhat small number of calibration fields is not unexpected considering

Field	r_1^{HZ09} [a]	90% (BS) [b] (mag)	I_{TRGB} (68% EDR) [c] (mag)	$(V-I)_{TRGB}$ [d] (mag)
19	1.02	0.01	$14.447^{-0.020}_{+0.028}$	$1.86^{+0.18}_{-0.21}$
11	0.12	0.01	$14.453^{-0.028}_{+0.042}$	$1.76^{+0.15}_{-0.18}$
33	0.68	0.01	$14.435^{-0.026}_{+0.026}$	$1.74^{+0.18}_{-0.18}$
32	1.09	0.02	$14.457^{-0.030}_{+0.026}$	$1.82^{+0.19}_{-0.24}$
13	0.32	0.02	$14.453^{-0.030}_{+0.024}$	$1.76^{+0.13}_{-0.15}$
29	0.62	0.02	$14.503^{-0.128}_{+0.052}$	$1.79^{+0.16}_{-0.20}$
18	0.31	0.02	$14.531^{-0.106}_{+0.014}$	$1.85^{+0.19}_{-0.24}$
27	0.95	0.02	$14.551^{-0.136}_{+0.026}$	$1.81^{+0.19}_{-0.19}$
28	0.77	0.03	$14.485^{-0.054}_{+0.142}$	$1.88^{+0.11}_{-0.28}$
5	1.14	0.03	$14.449^{-0.030}_{+0.062}$	$1.77^{+0.17}_{-0.21}$
17	0.37	0.03	$14.545^{-0.088}_{+0.018}$	$1.88^{+0.17}_{-0.18}$
25	1.18	0.04	$14.447^{-0.022}_{+0.100}$	$1.80^{+0.15}_{-0.21}$
23	0.37	0.05	$14.467^{-0.042}_{+0.118}$	$1.87^{+0.16}_{-0.20}$
6	1.73	0.06	$14.469^{-0.026}_{+0.126}$	$1.74^{+0.19}_{-0.17}$
14	0.48	0.06	$14.539^{-0.110}_{+0.060}$	$1.83^{+0.22}_{-0.22}$
30	0.60	0.10	14.509^{-nan}_{+nan}	$1.72^{+0.17}_{-0.15}$
31	0.83	0.11	14.417^{-nan}_{+nan}	$1.77^{+0.17}_{-0.20}$
26	1.95	0.12	14.735^{-nan}_{+nan}	$1.65^{+0.19}_{-0.14}$
22	1.48	0.13	14.515^{-nan}_{+nan}	$1.73^{+0.24}_{-0.20}$
15	1.58	0.14	14.451^{-nan}_{+nan}	$1.79^{+0.21}_{-0.23}$
8	1.36	0.17	14.815^{-nan}_{+nan}	$1.70^{+0.15}_{-0.15}$
7	1.62	0.20	14.671^{-nan}_{+nan}	$1.65^{+0.23}_{-0.13}$
10	1.34	0.24	14.965^{-nan}_{+nan}	$1.63^{+0.13}_{-0.13}$
16	3.24	0.31	15.037^{-nan}_{+nan}	$1.56^{+0.11}_{-0.11}$
1	0.88	0.37	14.465^{-nan}_{+nan}	$1.71^{+0.23}_{-0.15}$

Table 1.2: **TRGB quality metrics for the LMC Voronoi Fields**. This table is sorted according to the width (90% CI) of bootstrapped TRGB realizations for each field. Horizontal lines indicate the boundaries of each selection cut made to construct the calibration sample.
[a] Intermediate-age formation statistic. See Equation 1.2, 1.3.
[b] 90%-ile of bootstrapped realizations for each field. The table is sorted by this statistic.
[c] Modal value and 68%-ile of the edge detector response (EDR). A reliable TRGB value could not be determined for the 10 fields with the largest bootstrap uncertainty and the intervals are quoted as non-numbers to reflect this.
[d] 68%-ile of observed colors for stars in the magnitude interval $[I_{0,TRGB},\ I_{0,TRGB}+0.5$ mag$]$. Note that in the cases where a reliable Tip could not be located, this statistic will not meaningfully reflect a color at the TRGB. As a result, this column cannot be used for an accurate analysis of the TRGB's color dependence. See Figure 1.12 for a rigorous exploration of the TRGB's color dependence.

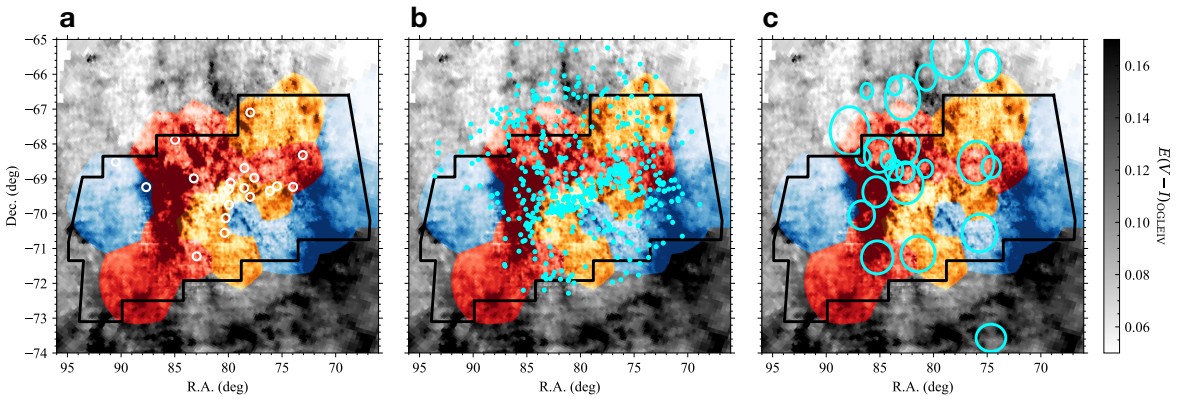

Figure 1.7: **Astrophysical Tracers of Star formation.** Objects that trace local star formation plotted on the OGLE-IV reddening map, with different colored regions corresponding to fields that were cut during the first set of selection cuts (red), the second set (orange), or retained to comprise the final calibration (blue). Grayscale intensity corresponds to the $E(V-I)$ reddening. **a,** DEBs (white)[42], **b,** Cepheids (cyan)[59], **c,** Supergiant shells (cyan).[30]

that the majority of the inner LMC is actively star-forming (see again Figure 1.3). Note also that the final calibration sample of five fields still covers more of the LMC than all prior spatially resolved analyses.[27, 17, 74, 56]

Figure 1.8 summarizes the TRGB measurement derived for the LMC. Panel (a) repeats the external map of dust reddening adopted for this study's reddening corrections. Regions are colored blue if the corresponding color-magnitude data are used in this study's final calibration, and red if excluded. Grayscale represents regions in the OGLE-IV map that fall outside the smaller OGLE-III footprint, which provides the publicly available photometry adopted for this study.

The TRGB measurement before imposing any selection cuts (Figure 1.8b) has a dominant discontinuity in the EDR at $I_0 = 14.44$ mag, with a tail of less significant edges that extends to fainter magnitudes. As shown in Figure 1.8c, applying the sample selection cuts considerably sharpens the dominant TRGB feature. The nominal TRGB magnitude is thus measured to be $I_0 = 14.439 \pm 0.005$ mag, with the uncertainty determined by bootstrapping the RGB LF.

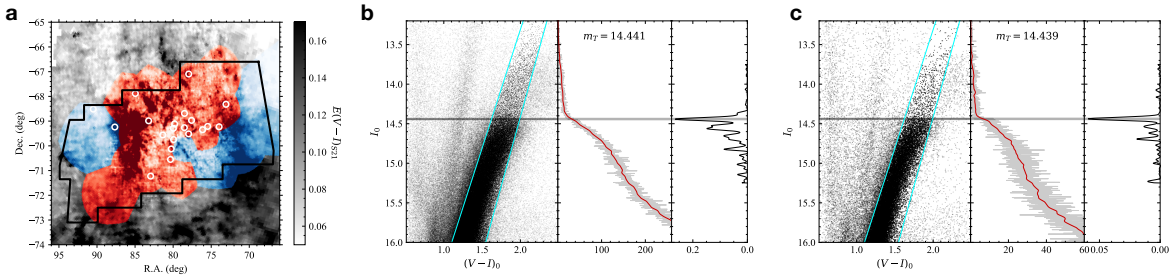

Figure 1.8: **TRGB measurement in the LMC. a,** Datasets underlying the TRGB measurements. Plotted is the reddening map from the OGLE-IV survey [55] that is used to de-redden the photometric measurements from the OGLE-III survey (its footprint plotted as a black outline) which are used in the TRGB analysis. Also plotted are the twenty DEBs (all aged < 2 Gyr) from the Araucaria Project[42] (white circles) which provide the trigonometric distance used to calibrate the TRGB luminosity. Spatial bins used to sub-divide the LMC are colored according to whether they passed (blue) or failed (red) the sample selection criteria. Note the spatial correlation between the young DEBs and the red regions. **b,** The color-magnitude diagram (CMD, left), binned and smoothed representations of the RGB luminosity function (LF, middle), and edge detector response (EDR, right) for the entire OGLE-III footprint of the LMC. The photometry is cleaned of foreground sources and corrected for dust reddening and variations in line-of-sight distance due to the on-sky tilt of the LMC. **c,** CMD, RGB LF, and EDR for just the adopted calibration sample (blue fields in Panel a). The likeliest TRGB magnitude is not measurably shifted from that identified in the full sample (panel b), demonstrating that the adopted sample selection amplifies the dominant TRGB signal already present in the unrestricted sample and is representative of the mean TRGB magnitude in the LMC. This conclusion is verified via subsampling experiments (see subsection 1.4.6).

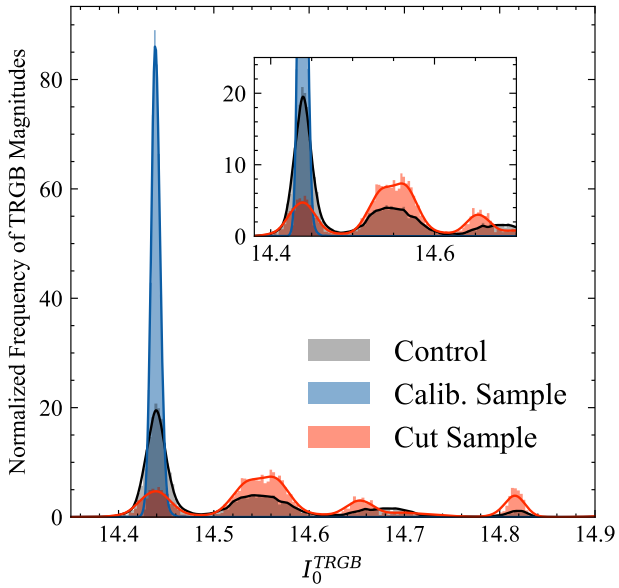

Figure 1.9: **Results from Subsampling Experiements. a,** The frequency of realized TRGB magnitudes when sampled from: the full OGLE-III footprint (gray, "Control"), only the calibrating sample (blue), and only the masked sample (red). The subsample size and edge measurement methodology are held constant for all realizations.

The TRGB discontinuity feature in the latter case is singular and unambiguous. The total width of the transition from the brighter Asymptotic giant branch (AGB) population to an RGB-dominated population (i.e., the TRGB feature) spans no more than 0.06 mag. Indeed, the contrast of the TRGB in the calibration sample is such that its magnitude can be identified to very high accuracy from visual inspection of the CMD alone. Note the location of the peak is identical to that seen in the full sample measurement, only that its location is determined to a higher precision. This indicates that the value of the TRGB determined from the calibration sample is not skewed by a potential selection bias. This assertion is verified via subsampling experiments.

1.4.6 Subsampling tests of LMC TRGB Measurements

The TRGB measurements in the LMC are further explored via subsampling experiments in which RGB stars are drawn from three samples: 1) The entire photometric footprint to serve

as a control, 2) the calibration sample, and 3) the clipped sample. The size of the subample drawn from all three is set equal to the size of the calibration sample (i.e., Figure 1.8c) to ensure that variations in number statistics do not affect the results.

It is confirmed that the calibration sample (blue distribution in Figure 1.9) produces a TRGB magnitude equal to but measured to higher significance than the already-dominant signal derived from the entire photometric footprint (gray distribution in Figure 1.9). This is consistent with inspection of the EDRs in Figure 1.8b,c. On the other hand, the clipped selection (Figure 1.9) undersamples the dominant peak and samples the broader, fainter peaks at a higher rate than the Control.

1.4.7 Measuring the On-sky Tilt of the LMC using the TRGB

A direct determination of the LMC geometry is made using TRGB magnitudes measured from 39 of 116 OGLE-III fields that exhibited single-peaked EDRs (shown in Figure 1.10). Note the spatial overlap with the main calibration sample from Figure 1.8 despite independent but similar sample selections. From these measurements, a strong signal of the geometric tilt is immediately apparent from the map of TRGB magnitude as a function of position in the galaxy (Figure 1.10a). A thin plane[38] is fit to this distribution of TRGB distances (Figure 1.10b,d). The residuals are convincingly de-trended (Figure 1.10c).

The resulting best-fit parameters for the position angle and inclination of the LMC plane ($\Theta = 153 \pm 12$, $i = 27 \pm 3$) are consistent with previous studies that used different astrophysical probes, including Cepheids[38], DEBs[42], Carbon stars[70], and RR Lyrae.[6] This provides additional evidence that the high-resolution OGLE-IV reddening map[55] accurately traces sight lines shared with TRGB stars (in regions of the LMC with a well-defined TRGB), and that the sample selection cuts are well-motivated. Otherwise the geometric signal would have contained more field-to-field scatter.

The effect of adopted center on the fit results is tested by considering a range of LMC

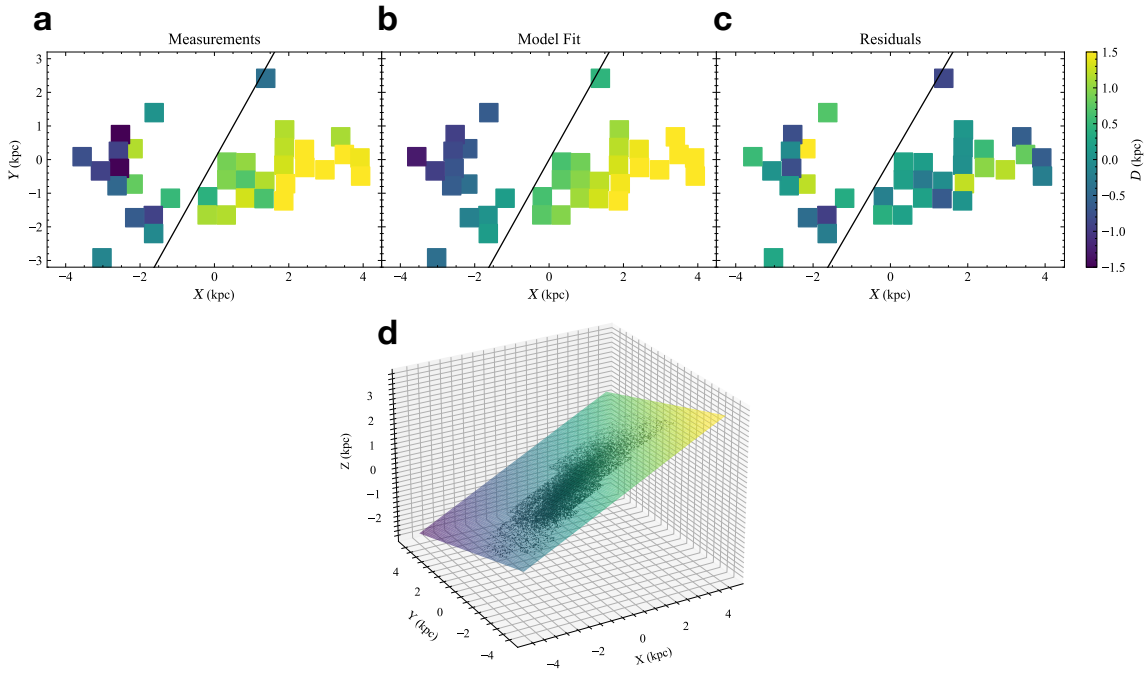

Figure 1.10: **Determination of the on-sky orientation of the LMC using the TRGB.** **a.** TRGB measurements made from the 39 adopted OGLE-III fields. **b.** Model predictions for the best-fit parameters $\Theta = 153 \pm 12°$, $i = 27 \pm 3°$. **c.** Residuals. The position of the best-fit line of nodes is plotted for reference. **d.** Three-dimensional visualization of the best-fit plane geometry, with the negative z-axis extending in the direction of the observer. A subset (20000 sources) of the total OGLE-III sample of RGB stars is overplotted (gray points).

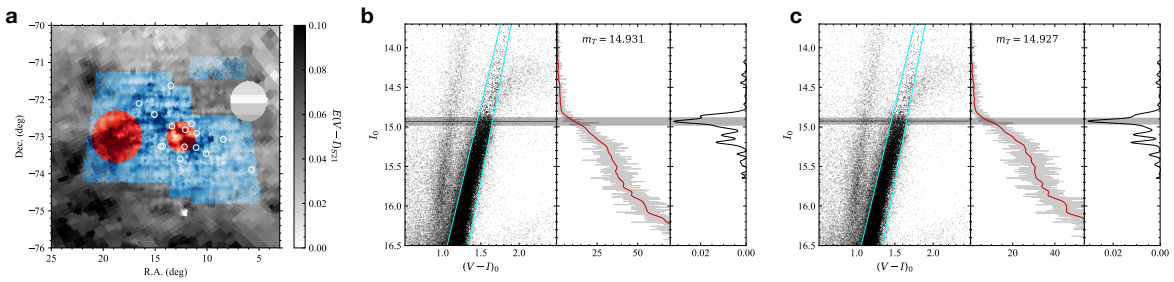

Figure 1.11: **TRGB Measurement in the SMC. a,** Field Selection as in Figure 1.8a, but for the SMC. The entirety of the OGLE-III footprint is adopted, with only the central star-forming region ($r_{GC} < 0.4$ deg) and the 0.7 deg centered on the star-forming Wing excluded from calibration. Again, the Araucaria Project DEBs[22] which provide the adopted trigonmetric distance are plotted (white circles). **b,** Same as Figure 1.8b but for the full OGLE-III footprint of the SMC. **c,** Same, but for only the calibrating sample (blue regions in panel a). As in the case of the LMC, the field selection does not introduce a significant shift in the measured TRGB magnitude, but does increase the precision in localizing its value.

centers derived from isophotes[8], infrared star counts[5] proper motions of young stars[71], and the distribution of RR Lyrae[6]. The maximal change to the best-fit parameters was only 1%, well within the $\sim 10\%$ uncertainties on the parameter estimates.

1.5 The TRGB in the SMC

All steps in the SMC TRGB measurement (Figure 1.11) are similar to the LMC one except that: 1) the SMC is not divided into individual spatial bins for a field-by-field analysis, and 2) line-of-sight geometric corrections are not applied. Both are not possible due to the SMC's extended depth along the line-of-sight, which introduces too much high-spatial-frequency stochasticity in the measured TRGB magnitudes (i.e., distance) for a reliable spatially-resolved analysis.

For the nominal SMC TRGB measurement (Figure 1.11), the full OGLE-III catalog is adopted except for the central 0.4 deg at $(\alpha_0, \delta_0) = (12.54, -73.11)$ deg and a 0.7 deg radius region centered on the Eastern Wing at $(\alpha_0, \delta_0) = (18.75, -73.10)$ deg (Figure 1.11a). Both regions are known to host relatively high levels of star formation.[50] The exclusion of

these small regions (containing only $\sim 20\%$ of the upper RGB stars covered by the OGLE-III footprint) from the calibrating sample sharpens the observed TRGB feature without significantly shifting its central value (Figure 1.11b,c).

The TRGB in the SMC follows a similar story to the LMC. The simpler sample selection here was designed to mask known star-forming regions of the otherwise quiescent SMC. Again, applying the selection (going from Figure 1.11b to c) sharpens the observed TRGB feature without significantly shifting its central value. This demonstrates the success of, and lack of observable bias in, the SMC calibration sample selection. The measured TRGB magnitude for the SMC is $I_0^{TRGB} = 14.927 \pm 0.023$ mag.

1.6 Absolute Calibration of TRGB Measurements

To build the next rung of the cosmic distance ladder, the dereddened TRGB measurements are brought onto an absolute system using the trigonometric DEB distances from the Araucaria Project.[42, 22] For the LMC, the calibration measurement (Figure 1.8c) is pegged to the DEB distance[42] to determine $M_I = -4.038 \pm 0.012_{\rm stat} \pm 0.032_{\rm sys}$ mag over the color range $1.60 < (V-I)_0 < 1.95$ mag. For the SMC (Figure 1.11c), the DEB distance[22] is used to determine the TRGB zero point over the color range $1.45 < (V-I)_0 < 1.65$ mag to be $M_I = -4.050 \pm 0.030_{\rm stat} \pm 0.039_{\rm sys}$. These absolute calibrations assume there to be no variation in the TRGB magnitude as a function of color over their narrow color ranges. They are tabulated in the first two rows of Table 1.3 with only their statistical uncertainties, with additional uncertainties discussed in .

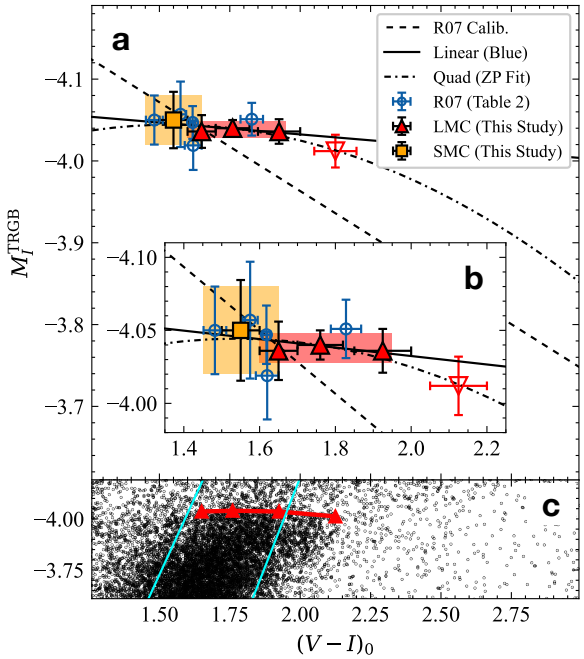

Figure 1.12: **Color dependence of the I-band TRGB**. **a,** Plotted are TRGB measurements from four color bins in the LMC (red triangles), the one measurement from the SMC (orange square), and TRGB zero point calibrators from Table 2 of Rizzi et al., 2007 (R07, blue circles). Filled points are used to fit for a linear dependence of the TRGB magnitude on color (solid black line) which is tabulated as Linear(Blue) in Table 1.3. The open red triangle is then included for the Linear(All) and Quad(ZP fit) fits. Also plotted are the flat zero point calibrations for the SMC (orange band) and LMC (red band). The VI slope of 0.217 mag mag^{-1} from R07 is plotted (dashed black line) and is a poor fit to the data. **b,** Inset that zooms on the TRGB measurements in the metal-poor/blue regime probed in this study. **c,** The CMD for the calibrating sample is shown with the corresponding color bin measurements (red triangles) and the color cut that was used for the flat TRGB measurement (cyan lines).

1.7 Exploring the Dependence of Intrinsic TRGB magnitude on Photometric Color

The magnitudes of TRGB stars are known to depend on their photometric colors, which is predominantly a metallicity effect.[7, 2, 69, 44] In the Johnson-Cousins I-band, the steepness of this TRGB magnitude-color relation still appears to be in question for metal-poor (blue) TRGB stars, with two commonly used calibrations diverging in this region of the CMD: a steep linear relation (hereafter referred to as R07)[48] and a shallower quadratic relation (hereafter referred to as JL17).[27] The new high-accuracy TRGB measurements in the MCs from this study can be used to address this question.

To determine the color dependence of the TRGB, the composite CMD of the calibration sample (Figure 1.8c, reproduced in Figure 1.12c) is divided into four color bins with a Tip magnitude measured from each (red triangles in Figure 1.12).

The color bins (horizontal error bars on red triangles in Figure 1.12) that define the LMC datapoints were varied in size and location. It was found that bins with widths smaller than the adopted ~ 0.15 mag were too sensitive to small shifts in the bin edges, which would have introduced a uniqueness problem into the color dependence fits. It is thought that this stochasticity in small color bins of the composite CMD is due to low number statistics, as well as residual white noise after application of the reddening and geometric corrections. Too narrow and a single color selection may be populated by RGB stars from only one spatial bin and thus only one set of corrections. So wide bin sizes are adopted to ensure the TRGB magnitude measured from each color bin reflects the mean population of TRGB stars in the calibrating sample.

For the TRGB measurement made from each color bin, all three sets of geometric corrections were considered, and the full range of measured TRGB magnitudes was added to the initial measurement uncertainty. This additional uncertainty was observed to increase for bluer color bins. This is expected because more metal-poor regions of the LMC are also

further from its center, and thus require larger line-of-sight distortion corrections. In other words, the bluest, outermost-located TRGB stars in the LMC do not provide as accurate of a constraint on the TRGB's color dependence as the inner regions.

Filling this gap at bluer colors, the composite SMC measurement (Figure 1.11b) is included, with the relative DEB distance uncertainty (0.017 mag)[22] added in quadrature to the TRGB measurement uncertainty (orange point in Figure 1.12). This leaves four datapoints with uncertainties between 0.015 mag (for the central LMC points) to 0.035 mag (for the SMC). Also in Figure 1.12, zero point calibration measurements from another study by Rizzi+07 (R07, blue points) are plotted along with the LMC and SMC zero points (red and orange bands, respectively).

Plotted in Figure 1.12 are TRGB magnitudes measured after dividing the LMC calibration CMD from Figure 1.8c into four color bins (red triangles), as well as one point (orange square) corresponding to the SMC measurement from Figure 1.11c. Also shown are Local Group dwarf zero point calibrators from the R07 study (open blue circles) and the R07 calibration of the I vs. $V-I$ magnitude-color relation (dashed black line). Fits to the TRGB magnitude and color measurements are also presented: a linear fit from this study (solid black line) to the blue TRGB points and a quadratic calibration from JL17 after having rescaled its zero point to best fit the data (dot dashed curve). These fits are tabulated in Table 1.3 along with the earlier calibrations that assumed a color-invariant TRGB magnitude over their color ranges (shown as rectangular bands).

When excluding the reddest color bin of the LMC measurements, no evidence (a p-value of 0.42) is found for a TRGB color dependence (0.018 ± 0.018 mag mag^{-1}), which is tabulated as "Linear (blue)" in Table 1.3 and plotted as a black solid line in Figure 1.12. When including the reddest datapoint, stronger evidence (p-value of 0.07) is found for a shallow slope (0.053 ± 0.019 mag mag^{-1}), while the RMS scatter increases from 0.004 mag to 0.006 mag.

Type	c_{min}	c_{max}	Parameter Values and Errors	p-value	RMS
Flat (SMC)	1.45	1.65	$-4.050(\pm0.023)$	N/A[b]	N/A[b]
Flat (LMC)	1.60	1.95	$-4.038(\pm0.005)$	N/A[b]	N/A[b]
Linear(Blue)	1.60	1.95	$-4.040(\pm0.002) + 0.018(\pm0.018)(c - 1.75)$	0.42	0.004
Linear(All)	1.45	2.20	$-4.037(\pm0.003) + 0.053(\pm0.019)(c - 1.80)$	0.07	0.006
Quad (ZP)[a]	1.45	2.20	$-4.045(\pm0.002) + 0.091^{a}(c - 1.5)^2 - 0.007^{a}(c - 1.5)$	N/A[c]	0.004

Table 1.3: **Final TRGB Calibrations**. c in all cases is a placeholder for $(V - I)_0$. Only statistical/formal uncertainties are quoted here. The full error budget for each zero point is presented in chapter 2. Note the different pivot colors adopted for each of the Linear and Quad calibrations. The Quad calibration is preferred and bolded.
[a]Only the intercept of this relation was fit for in this study. The color terms were adopted directly from Jang & Lee (2017)[27] and allowed to vertically rescale to best fit this study's TRGB measurements of the Clouds. The reader is referred to that study for uncertainties on the adopted curvature parameters and for transformations to HST bandpasses.
[b]There is no p-value or Fit RMS for the Flat calibrations, because they were determined from a nonparametric edge detection, and not from a minimization of a parametric model's residuals.
[c]There is no p-value for the Quad calibration because only the zero point was fit for, with the color terms adopted from an external study (see note a).

The JL17 quadratic calibration, after re-fitting for only the vertical intercept of their QT relation, provides the best fit (RMS = 0.004 mag) to the full color range of TRGB measurements, while the R07 equation produces an order of magnitude larger scatter (RMS = 0.033 mag) and is not considered further. The poor fit of the R07 slope is likely caused by an issue in their transformation from space to ground filter systems, because the other TRGB slopes determined by R07 in the Hubble Space Telescope (HST) filter sets are consistent with the analogous equations presented in JL17. Both studies performed their color calibrations in the native HST filters then later transformed to ground-based magnitudes.

Note the quadratic terms were not newly fit for here and only the intercept was allowed to vary, meaning the external JL17 model *predicts* the TRGB color dependence observed in the Clouds to millimag (sub-percent) precision. The updated QT zero point, along with the JL17 color terms are included as the last entry in Table 1.3. This is the author's recommended calibration and is valid over the full MC TRGB color range $1.45 < (V - I)_0 < 2.20$ mag.

It is important to consider the universality of the newly presented calibrations. A long-

standing question of the TRGB concerns the extent to which differences in stellar age might systematically alter the color-metallicity relation of TRGB stars, potentially breaking the assumed universality of a proposed color calibration.[52] Encouragingly, in this section it was shown that the quadratic color dependence adopted from JL17—which they determined from observations of the outer regions of L_* galaxies—describes very well the TRGB magnitude-color relation of the MCs measured in this study and that of the Local Group dwarfs from R07.[48] This consistency indicates that for RGB stars found in these environments either: the age distributions overlap considerably (i.e., galaxy stellar halo populations resemble those of satellite dwarfs), or age-dependent variations in the I-band TRGB magnitude are minimal (which is a consistent result from stellar evolution theory). In either case, the I-TRGB appears well-behaved and without a measurable bias across these host environments. Conversely, the present calibration should only be used to measure distances to similar environments.

1.8 Understanding the Disagreement over the Measured Brightness of the TRGB in the Clouds

Depicted in Figure 1.13a are previous calibrations of the TRGB in the literature that were derived using the same photometric measurements of the LMC that were used in this study, but under different assumptions about the dust reddening. This includes JL17, Gorski+18 (hereafter G18)[17], Yuan+19 (hereafter Y19)[74], Freedman+20 (hereafter F20)[13] and Soltis+21 (hereafter S21).[56]

In Table 1.4 each of the studies' originally presented TRGB zero point is included in the left-most column. See chapter 3 for reproductions of each independent study (this excludes Y19 and S21 which did not make new TRGB measurements). The second column of Table 1.4 shows the same TRGB values after having been renormalized to the same assumptions on distance and dust reddening that were adopted for this study, enabling direct comparison

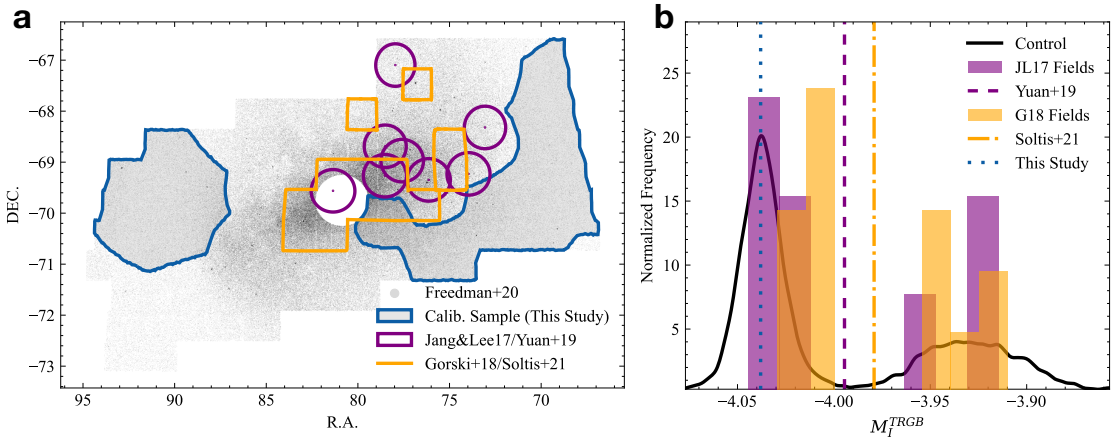

Figure 1.13: **Addressing Disagreement over Measuring the TRGB in the LMC. a,** The on-sky locations of all recent calibrations in the LMC (tabulated in Table 1.4) are plotted over a source density map of Upper RGB stars ($V - I > 0.5$ mag, $I < 17$ mag) in the LMC (black points). The Jang&Lee (2017) (purple circles with dots)[27] measurements were directly adopted and post-processed by Yuan+19[74] so they share footprints. The same is true for the Gorski+18 measurements (orange rectangular outlines)[17] which were adopted and post-processed by Soltis+21.[56] The inner 1 deg is excised as done in the Freedman+20 calibration (all black points). This study's calibration sample is also shown (blue outline). Note the JL17 fields overlap considerably and their representation here is decreased in radius by a factor of two for clarity. **b,** Histograms (colored rectangles) of TRGB measurements derived from the individual JL17/Yuan+19 (purple) and G18/Soltis+21 (orange) fields scaled to an arbitrary height. The simple weighted average values adopted by Yuan+19 and Soltis+21 are plotted as vertical dashed and dot-dashed lines, respectively. Both studies adopted 0.01 mag as the uncertainty on their mean TRGB measurements. Also shown is the distribution of TRGB magnitudes measured from subsampled realizations of the unrestricted LMC photometric catalog (no sample selection made), referred to as "Control" (solid black curve, see Figure 1.9), along with the nominal measurement from this study (blue vertical dashed line).

Reference	$M_{I,TRGB}$ (original)[a]	$M_{I,TRGB}$ (renormalized)[b]	Measurement Method	Color Correction
Jang & Lee (2017)	-3.970 ± 0.090	-3.993 ± 0.059	Field-by-field Average	Blue Selection
Jang & Lee (2017)	-3.998 ± 0.082	-4.020 ± 0.046	Field-by-field Average	Quadratic
Gorski+18[c]	-4.088 ± 0.011	-3.997 ± 0.011	Field-by-field Minimization	Linear
Yuan+19[d]	-3.952 ± 0.046	-3.991 ± 0.027	Field-by-field Average	Blue Selection
Freedman+20[e]	-4.047 ± 0.034	-4.018 ± 0.028	Composite CMD	Blue Selection
Soltis+21[f]	-3.960 ± 0.011	-3.960 ± 0.011	Field-by-field Average	None
This Study				
	...	-4.038 ± 0.005	Composite CMD	Blue Selection
	...	-4.036 ± 0.003	Composite+Color bins	Linear
	...	-4.036 ± 0.002	Composite+Color bins	Quadratic (ZP Fit Only)[g]

Table 1.4: **Compilation of LMC-based TRGB Calibrations**. Note: Zero points of sloped calibrations were extrapolated to the average LMC TRGB color in each dataset.

[a]Values from original studies are quoted without DEB distance uncertainties, since all studies adopted either the 2013 or 2019 value of the Araucaria Project's DEB distance to the LMC, but adopted different sets of reddening corrections[24, 18, 55], or, in the case of F20, presented a direct reddening determination.

[b]Renormalized values indicate that both reddening and geometric distance assumptions are homogenized to the latest Araucaria Project distance[42] and the OGLE-IV reddening map[55]. These values are thus quoted without either geometric distance or reddening uncertainties.

[c]Values quoted in their Figs. 6-8 could not be reproduced from the accompanying tables. See chapter 3 for this author's attempted reproduction of their result based on their Tables 2 and 3, which is the source of this quoted value. This study did not present an error budget beyond the standard errors on the fit parameters, so the quoted uncertainties are smaller than others in the table.

[d]Adopted Blue-TRGB measurements from JL17, but not their uncertainties.

[e]Performed a mean reddening correction, not a spatially dependent one as done in JL17, G18, and this study.

[f]Adopted mean of raw G18 TRGB measurements. Did not control or correct for metallicity/color as was done in the original study.

[g]Quadratic color dependence adopted from JL17[27] with zero point updated in this study (Figure 1.12).

between just the TRGB measurements. Comparing the renormalized TRGB values highlights that the disagreement over TRGB calibration in the LMC goes beyond the assumptions made of the dust reddening, and is equally tied to a significant disagreement over the brightness of the TRGB as measured directly from the same OGLE-III star catalog.

The underlying reason for this discrepancy is demonstrated in Figure 1.13b. In it, the two recent studies that presented very faint and low-uncertainty measurements of the LMC TRGB relative to the rest of the literature (Y19 and S21) are compared to the distribution of TRGB magnitudes determined in this study from the entire OGLE-III footprint (i.e., no selection cuts applied). This Control distribution was computed by subsampling with replacement the RGB LF from Figure 1.8b to match the sample size of the calibration sample in Figure 1.8c. It is apparent that the JL17 and G18 measurements adopted by Y19 and S21 sampled from a broader, secondary peak in the distribution of bootstrapped TRGB magnitudes at a higher rate than Control. This introduces an artificial bimodality into the TRGB measurements for these studies that is not representative of the LMC as a whole (as traced by the Control distribution).

Y19 and S21 averaged over this bimodality and estimated the uncertainty as the standard error on the mean of a univariate Gaussian distribution, which is not a valid assumption. As a result, these studies suffer from at least a ~ 0.05 mag (2% in distance and in units of H_0) bias that is not accounted for in their proposed calibrations of the TRGB distance scale. [74, 56] See chapter 3 for why S21 suffers from an additional 0.04 mag bias due to unaccounted-for metallicity effects.

1.9 Discussion

To highlight the consistency of the new TRGB measurements presented in this study, we compare the TRGB constraint on the relative distance modulus $\Delta\mu$ between the LMC and SMC to that derived independently from the DEBs. Differencing the flat LMC and SMC mea-

surements suggests $\Delta\mu = 0.488 \pm 0.024$ mag. Applying the quadratic JL17 color correction to each galaxy's measurements results in $\Delta\mu = 0.494 \pm 0.024$ mag. Both values are in excellent agreement with the independent constraints from the DEBs, $\Delta\mu = 0.500 \pm 0.017$ mag. The remarkable consistency between this study's TRGB measurements and the geometric DEB distances provides an important check on the accuracy of the presented analysis and highlights our increasingly accurate understanding of the MC system as a whole.

After applying motivated sample selection cuts, the brightness of the TRGB in each of the LMC and SMC was measured to its highest precision and accuracy to date. The color dependence of the TRGB over the range of colors seen in the MCs was small and best described by the external quadratic calibration presented in JL17. The TRGB was also used to constrain the on-sky tilt of the LMC as well as the distance between the Small and Large Clouds. Both results are in total agreement with the constraints based on the DEBs and provide a compelling check on the self-consistency of this study's TRGB measurements. Debate over the brightness of the TRGB in the Clouds appears to be resolved and the precision of the TRGB zero point calibration is improved to sub-percent precision in statistical uncertainty.

CHAPTER 2

ERROR BUDGET

The additional error budget of the TRGB calibration is discussed here and tabulated in Table 2.1, with separate columns for calibrations based in either the Large or Small Cloud. In addition to the formal uncertainties on individual calibration zero points (parentheticals in Table 1.3), a number of additional uncertainties are quantified or, in the case of the external reddening and distance uncertainties, propagated from the original studies.

The dominant uncertainties in the LMC error budget are systematic uncertainties associated with the DEB distance (0.026 mag) and the adopted reddening corrections (0.017 mag). The dominant uncertainty in the SMC calibration is statistical in nature and is due to the galaxy's measurable line-of-sight depth, which manifests as a vertical blurring of the SMC's TRGB feature (see again Figure 1.11b,c). The size of the effect naturally arises in the TRGB measurement uncertainty (0.023 mag) and the statistical uncertainty on the DEB distance (0.019 mag), both of which are about a factor of five times larger than their respective quantities in the LMC calibration.

Error Term	LMC		SMC	
	stat. (mag)	sys. (mag)	stat. (mag)	sys. (mag)
Sample Selection	0.005	0.002	0.007	0.01
Extinction	0.006	0.017	0.004	0.022
DEB Distance	0.004	0.026	0.019	0.028
Photometry	0.004	0.01	0.004	0.01
Combined Uncertainties	0.010	0.033	0.021	0.038

Table 2.1: **Additional Uncertainties in the TRGB Zero point Calibration.** Uncertainties here are to be added in quadrature to the formal zero point uncertainties quoted in Table 1.3. The LMC quantities are to be used for all calibrations of Table 1.3 except for Flat (SMC).

2.1 Sample Selection

To estimate statistical uncertainties in the LMC calibration due to sample selection, the fields in the calibration sample are jack-knife resampled to potentially identify anomalous detections. The final TRGB magnitude is robust to resampling at the 0.005 mag level, and that value is adopted as a statistical uncertainty. In the case of the SMC, the masked inner region boundary is varied from $r = 0.2$ deg to $r = 1.0$ deg, with the full range of measured Tip values spanning 0.007 mag. That value is adopted as a statistical uncertainty under "Sample Selection" in Table 2.1. Varying the boundary of the also-masked Wing region of the SMC over the same range of radii had no effect on the measured TRGB magnitude.

The effect of a radial cut (varied between 0 and 1 deg) on the LMC calibrating sample was also tested, with no change observed in the measured TRGB magnitude.

In the case of the SMC, there is a substantial uncertainty due to its back-to-front depth. In a recent study,[35] RR Lyrae were used to determine the line-of-sight depth of the SMC's spheroidal component to be 4 kpc ($\pm$0.14 mag) which places an absolute upper limit on our ability to converge on a central value for the mean distance to the SMC. If we assume one TRGB star provides an independent sampling of the mean SMC distance distribution, then the uncertainty due to back-to-front depth can be estimated via the standard error, i.e., $0.14/\sqrt{(168)} = 0.011$ mag where the number of TRGB stars was estimated by selecting for TRGB stars within 0.02 mag of the adopted Tip magnitude. The existing uncertainties on the Tip detection (0.023 mag) and DEB distance (0.019 mag) more than encompass this estimate on the uncertainty due to line-of-sight depth.

2.2 Geometry

In the case of the LMC, the effect of adopted plane geometry, from which distortion corrections were applied on a star-by-star basis, was also considered. Using any of the three sets

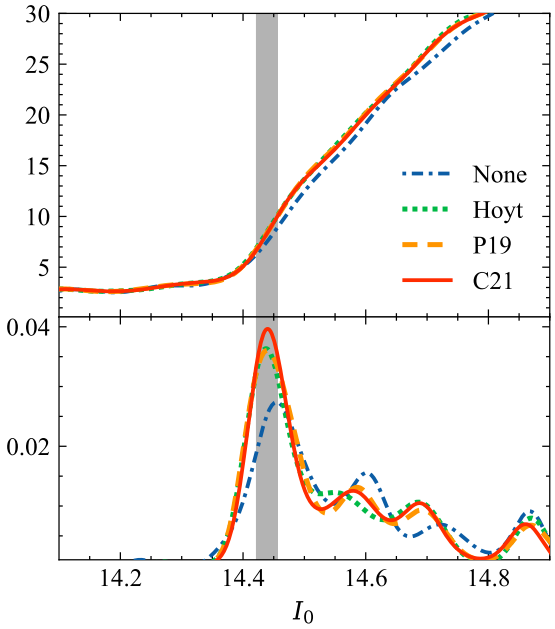

Figure 2.1: **Comparison of Geometric Correction Models.** Comparison of RGB LFs and EDRs resulting from the three different sets of geometric corrections derived from: RR Lyrae (C21, red solid curves)[6], the DEBs (P19, orange dashed curves)[42], and this study's TRGB measurements (Hoyt, green dotted curves). All three return consistent TRGB edge locations which are sharper than the measurement without geometric corrections (None, blue dot-dashed curves). The corrections based on the RRL-derived geometry (see text) produce the sharpest edge feature and that set is adopted for the final calibration. The 2σ band representing the nominal statistical uncertainty $\sigma = 0.005$ mag is plotted for reference.

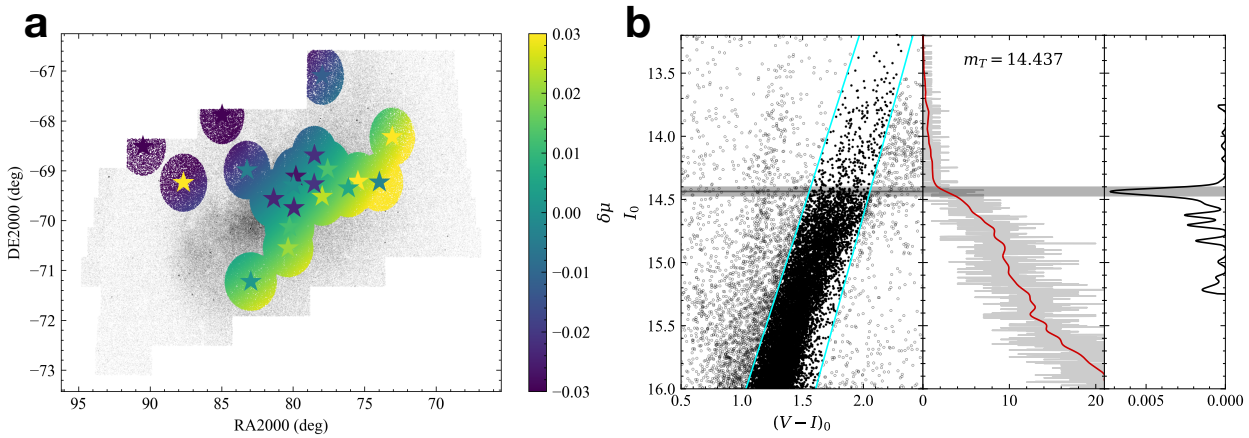

Figure 2.2: **TRGB measurement using model-independent corrections for the LMC's tilt. a,** Twenty $r < 35'$ fields (circles of colored points) centered on the DEBs (colored stars) are constructed and *empirical* (model-independent) geometric distortion corrections are computed for each source equal to the distance measured to the DEB at the center of its respective field. For sources contained in multiple DEB fields, a weighted (inverse variance) average of the associated DEB distances is used. The rest of the sources in the LMC photometry are also plotted (black points). The DEB stars are colored according to their offset in distance from the mean value in P19 ($\mu = 18.477$ mag) while the sources in the circular regions are colored according to the modeled corrections that were adopted for the main analysis. **b,** The sample is then convolved with the main analysis calibration selection (blue fields in Figure 1.8a). The agreement with the primary result (Figure 1.8b,c) confirms that the modeled line-of-sight depth corrections adopted for the LMC calibration are accurate. The 0.002 mag difference is folded into the error budget.

of geometric corrections result in TRGB magnitudes all consistent to within 0.002 mag (Figure 2.1). Furthermore, in Figure 2.2, a TRGB measurement made using a *model-independent* set of line-of-sight depth corrections is within 0.002 mag of the result using modeled corrections. This value is adopted as a systematic uncertainty in the "Sample Selection" row of Table 2.1.

An additional uncertainty in the SMC is explored by considering the effect that choice of adopted center has on the final TRGB magnitude (since the innermost region is masked). The adopted SMC center is varied between a range of values from the literature[5, 47, 35] and the full range of measured TRGB magnitudes (0.01 mag) is adopted as an uncertainty. This value is tabulated under the "Sample Selection" row in Table 2.1 as a systematic.

2.3 Extinction/Reddening

To estimate the statistical uncertainty due to adoption of the OGLE-IV reddening map[55], their σ_1 and σ_2 quantities are used. These quantities are intended to characterize the amplitude of back-to-front differential reddening inherent to each pixel, i.e., the statistical uncertainty associated with discretely sampling the distribution of dust along LMC sight lines. To quantify the effect this uncertainty has on the final zero point calibration, the peak of the σ_1 distribution for the calibrating sample of TRGB stars (determined by selecting for stars within 0.02 mag of the adopted TRGB magnitude) is divided by the square root of the sample size, resulting in $0.065/\sqrt{156} = 0.005$ mag for the LMC and $0.05/\sqrt{168} = 0.004$ mag for the SMC. These quantities, after conversion to A_I, are included as statistical uncertainties in the Extinction row of Table 2.1.

The dominant uncertainty in the reddening lies in its zero point. Systematic uncertainties on the zero point of 0.014 mag and 0.018 mag are adopted for the LMC and SMC, respectively. These values are taken directly from the *total* RMS scatter in the OGLE-IV calibration of the RC mean color, which used the SFD98/SF11 dust maps, as well as an em-

pirically calibrated RC color vs. galactocentric radius relation, to determine the RC intrinsic color throughout the MCs. This ensures that their reddenings are on the same system as the widely-used SFD98/SF11 foreground dust maps and places this study's TRGB calibration on the same extinction zero point as any TRGB measurement to which only integrated foreground reddening corrections are required (e.g., in the SN Host stellar halo imaging that calibrates the TRGB-SN H_0).

The color-metallicity relation of the RC plays an important role in the OGLE-IV reddening maps, especially since it is required to extrapolate the RC intrinsic color from the outer regions of both Clouds (where they could calibrate directly to the SFD98/SF11 maps) to the inner regions like those used for the present TRGB calibration. To perform this extrapolation, they measured two empirical relations: a metallicity-radius relation for each Cloud and a color-metallicity relation for RC stars. Notably, both of these were determined empirically with measurements made in the MCs themselves (spectroscopic metallicities of red giants and star clusters paired with OGLE-IV photometry). Also, the RC color-metallicity relation from the OGLE-IV map[55] differs by no more than 0.02 mag from a recent theoretical prediction[36] at either end of the LMC's metallicity range, suggesting the dependence of the RC color on metallicity is well-behaved. It is thus concluded that the current adopted systematic reddening uncertainties (again, taken to be the *full* scatter in the $(V-I)_{RC}$ vs. $E(V-I)_{SFD98/SF11}$ vs. radius relation for each Cloud) sufficiently account for uncertainties in the RC color-metallicity relation. Furthermore, any systematic effect on the RC intrinsic color due to an age dependence of the RC intrinsic color is minimized in this study because only regions with well-defined TRGB features have been considered. Because the TRGB also requires a pristine, older population of stars, it becomes likelier that the RC stars that coincide with the TRGB calibration sample will be similar to the RC population that makes up the intrinsic color calibration in the quiescent outer regions of each Cloud.

2.4 Photometry

In the case of the LMC, there exist two OGLE photometric catalogs, the primary photometric maps[65] and the OGLE-Shallow survey,[68] both of which have been used in prior studies of the LMC TRGB. The two result in slightly different (0.004 mag) final TRGB calibration results and that quantity is adopted as an additional statistical uncertainty (since there is no clear choice of which photometry might set the "true" baseline). The same quantity is also propagated to the SMC, despite the lack of an equivalent "Shallow" catalog to perform the same comparison. Lastly, a systematic uncertainty equal to 0.01 mag is adopted for both galaxies based on the OGLE collaboration's preferred uncertainty on their photometric zero points.

CHAPTER 3

REPRODUCTIONS AND RENORMALIZATIONS OF LITERATURE STUDIES

In this chapter, the literature studies discussed in the main text are reproduced, if possible. To enable congruous comparison with the TRGB calibration determined in this study, each of the literature studies' results are rescaled onto the OGLE-IV reddening map[55] and the latest DEB distances from the Araucaria Project.[42, 22]

3.1 Notes on Geometric Corrections in Pietrzynski+19

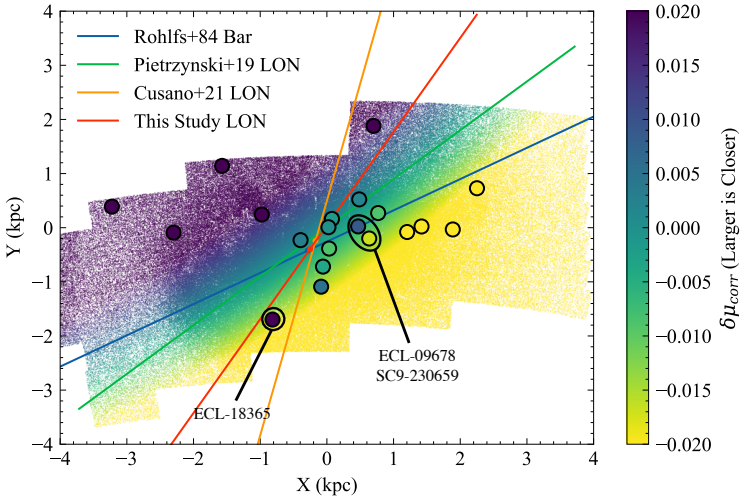

Figure 3.1: **Geometric Correction Models and the P19 DEB Distances.** Upper RGB ($V - I > 0.5$ mag, $I < 17$ mag) stars from OGLE-III are plotted and colored according to their associated geometric distortions, as computed with Equation 1.4 and the fit parameters from P19. Also plotted are the 20 DEBs from P19, color-coded according to the "corr" values tabulated in their Table 1. The lines of nodes from P19, C21, and this study are plotted (green, orange, and red lines, respectively). For reference, the position angle of the Bar as determined from HI observations[49] is plotted (blue line). DEBs with anomalous "corr" values in P19 Table 1 are annotated and discussed in the text. Equatorial coordinates are converted to physical, Cartesian coordinates using $\mu = 18.477$ mag.[73] Note the inverted scale as compared to Figure 2.2. This inversion is to be consistent with the P19 representation of the geometric distortions as *corrections* to be made, rather than measured distances.

During computation of the geometric distortion corrections (see again subsection 1.2.4), it was noticed that the "corr" values contained in Table 1 of the DEB distance paper [42, hereafter P19] do not appear consistent with the predictions from their best-fit planar model of the LMC disc. To illustrate this point, the DEBs ECL-09678 and SC9-230659 are highlighted in Figure 3.1a. The two DEBS are in very close proximity to each other (separated by only $19'$) but are tabulated in the original P19 Table 1 as having *predicted* line-of-sight corrections that differ by 0.026 mag (or 0.59 kpc at a distance 50 kpc), a gradient that far exceeds all known measurements of the LMC's on-sky tilt. Another illustrative outlier is ECL-18365 which, according to its listed coordinates, is located on the more distant, SW side of the line of nodes, while the P19 "corr" value states that it is predicted to be 0.033 mag *nearer*. It is not possible for a smooth planar model to produce these high-frequency variations in predicted line-of-sight distance.

Summarizing the situation, it was found that the standard deviation of the DEB distances in P19 increases from $\sigma_\mu = 0.026$ mag without any geometric corrections applied to $\sigma_\mu = 0.028$ mag, after adding the "corr" values quoted in P19 Table 2. Conversely, if the corrections are instead re-computed here using Equation 1.4 and the P19 planar fit parameters ($\Theta = 132^\circ$, $i = 25^\circ$), the dispersion in the distortion-corrected DEB distances decreases as expected to $\sigma_\mu = 0.022$ mag, which is closer to the typical uncertainty quoted for each DEB distance measurement ($\sigma = 0.019$ mag). It would appear that the parameters quoted for their LMC planar fit were reported accurately, but some minor inconsistencies were introduced in the presentation of the data (their Table 1 and Figure 2). The source of the inconsistency is unclear but from this analysis it becomes clear the issue was introduced in post-production and did not affect their results.

In any case, the actual effect on computing the mean distance to the LMC is trivial. When using any of the three sets of DEB distances— (1) with no geometric correction, (2) after applying the apparently inaccurate corrections tabulated in the "corr" column of P19

Table 2, or (3) using the updated and accurate P19 geometric corrections re-computed here —the maximal difference in the mean LMC distance is only 3 mmag.

3.2 JL17/Y19

3.2.1 Original Study

After calibrating the run of the I-band TRGB magnitude with VI color (see again Figure 1.12), JL17 measured the TRGB in $r \leq 50'$ fields centered on the eight DEBs that defined their adopted distance.[41] They used RC reddening maps calibrated to a theoretical intrinsic color calibration[24] and the DEB distance (and accompanying geometric corrections)[41] to bring their TRGB measurements onto an absolute system and determine a TRGB zero point. They provided two calibrations based in the LMC: a "blue-TRGB" which selected for only metal-poor TRGB stars, $M_I = -3.970 \pm 0.102$ mag and a calibration using their externally-determined quadratic color correction ($M_I = -3.998 \pm 0.096$ mag for $(V-I)_0 = 1.80$ mag). These calibrations are tabulated in the first two rows of Table 1.4 with the DEB distance uncertainties subtracted out.

Looking at the measurements made by JL17 (their Figure 10 and Table 5), there is an apparent internal discrepancy between the individual QT and "blue TRGB" measurements for their eight EB fields. As an introduction, the blue edge of their RGB selection box for the blue-TRGB measurements was positioned at $(V-I)_0 = 1.5$ mag, exactly at the pivot color of the QT correction (pictured in Figure 1.12). Thus, all of their QT corrections in the LMC should have monotonically brightened the TRGB magnitudes by a predictable amount based on the mean color of TRGB stars in those fields. This however was not always the case. For example, their field EB8 TRGB measurement became 0.05 mag *fainter* after the QT color correction, which should not be possible. Similarly, fields EB6 and EB7 both became 0.08 mag brighter when measured in the QT-rectified CMD. However, if one

directly computes the expected color-correction based on their QT function (see Quad row of Table 1.3), the exact correction values are 0.027 mag and 0.017 mag, for mean colors $(V-I)_0 = 2.00$ mag, and $(V-I)_0 = 1.90$ mag, respectively. This inconsistency between the QT and blue TRGB detections is likely real and a reflection of the ambiguous nature of the TRGB detections in those fields. Put another way, even small percent-level modifications to the stellar magnitudes (via color-rectification) and sample selection (color selection box) can introduce 5-10% discrepancies in the measured TRGB magnitude, up to a factor of four larger than expected and the level of the disagreement that motivated this study. This will now be confirmed.

The TRGB is re-measured to each of the JL17 fields and it is found that the EDRs for five of the eight DEB-centered fields exhibit strongly bimodal responses, similar to those cut in stage 2 of the selection cuts (Figure 1.6). Only three of eight JL17 fields were found to exhibit clear, unambiguous TRGB measurements: EB4, EB7, and EB8. My measurements to these fields are in excellent agreement with those of JL17 (after correcting for differences in reddening), except for the TRGB measurement to EB7 for which I find an unambiguous bright peak 0.10 mag brighter than that measured by JL17. Notably, the five low-quality fields overlap considerably (as was shown in Figure 1.13 near $\alpha = -77^\circ, \delta = -69^\circ$), so the bimodal feature is likely sourced by the same local stellar population. Indeed, the overlap is so considerable that there are 640000 sources contained in total across all eight fields (including overlapping sources). That number decreases to 340000 after exclusion of duplicates.

To illustrate the bimodality in the JL17 measurements the TRGB was measured to the eight JL17 fields in two ways: allowing the edge detector to trigger anywhere, and where it was forced to trigger on the brighter of the two observed peaks. From the former unrestricted analysis, the mean TRGB was found to be 14.50 ± 0.040 mag, while the latter set the mean TRGB magnitude is 14.46 ± 0.011 mag, where the quoted error bars are the total dispersion. The former is identical to what JL17 originally measured to their eight fields (after taking

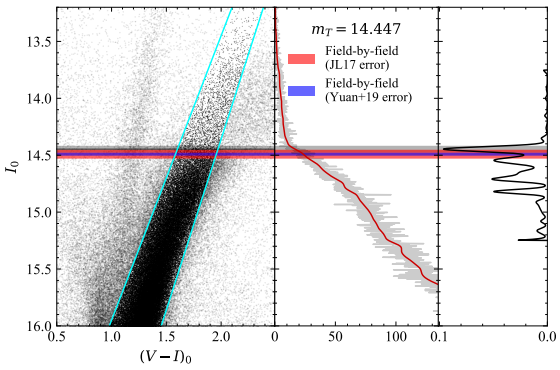

Figure 3.2: **Composite CMD Measurement from the JL17 sample.** Instead of considering each of the eight, $r < 50'$ DEB-centered fields separately as done by JL17 and Y19, a composite CMD is formed from the set union of the eight fields. The field-by-field average and uncertainty adopted by JL17 (red band) and Y19 (blue band) is shown. The choice made by Y19 to reduce the JL17 uncertainties makes the bias in the field-by-field average statistically significant. The composite CMD approach aggregates power in what is ostensibly the true, constant-luminosity TRGB which produces an unbiased final result; the biased TRGB features only add noise and a long tail of smaller peaks in the EDR.

into account the updated DEB distances and reddening map). In the latter case, the smaller scatter and brighter mean magnitude would suggest that the brighter of the two peaks likely represents the true TRGB magnitude in each field. Crucially, the authors noticed this bimodality and adopted an appropriately large uncertainty (0.04 mag uncertainty on the average and an additional 0.02 mag to account for intermediate-age contamination).

Later, Y19[74], however, in their adoption of the central values of the JL17 blue-TRGB measurements, did not also propagate the JL17 uncertainties, thereby increasing the statistical significance of this bias in their proposed calibration. Y19's calibration $M_{F814W} = -3.97 \pm 0.046$ mag is shifted back to $M_I = -3.952 \pm 0.046$ mag by their measured ground-to-HST offset $I - F814W = 0.018$ mag. This value is entered in the fourth row of Table 1.4.

Furthermore, if the TRGB is measured from a composite CMD constructed from the set union of the eight JL17 DEB fields, then the bias in their field-by-field average calculation (red band in Figure 3.2) is weakened, with the source of the bimodality in their individual measurements also identified (note how the field-by-field average sits in the middle of two

peaks). Again, the uncertainty from Yuan+19[74] is confirmed to be a significant underestimate of the underlying distribution (blue band Figure 3.2). The value $I_0 = 14.447 \pm 0.02$ mag determined from this approach (gray band) is in agreement with the result from this study.

3.2.2 Renormalization to Homogeneous Reddening and Distance Measurements

To accurately compare the original JL17 results with this study's results, the JL17 zero points are shifted by the average offset between their adopted RC reddening map[24] and the OGLE-IV[55] reddening map adopted for this study ($\Delta E(V-I) = +0.032$ mag).[55] The zero point is also updated from the old DEB distance from the Araucaria Project[41] to the latest distance $\Delta\mu = +0.016$ mag[42]. Their blue-TRGB calibration becomes $M_I = -3.993 \pm 0.059$ mag and the QT zero point becomes $M_I = -4.020 \pm 0.046$ mag, where the extinction and distance uncertainties have been subtracted out. These renormalized zero points are tabulated in the second column of Table 1.4 under the "Renormalized" block and are consistent with this study's measurements to within the uncertainties.

The Yuan et al.[74] zero point is also shifted by the average offset between the two reddening maps, giving $M_I = -3.991 \pm 0.027$ mag. They had already updated the JL17 calibration to the latest DEB distance.

3.3 G18

3.3.1 Original Study

G18 presented a multi-wavelength calibration of the TRGB magnitude using a selection of 14 (out of 116 available) centrally located, metal-rich fields. They determined a TRGB zero point of -4.119 ± 0.008 mag at $(V-K)_0 = 3.8$ mag. After extrapolating to the mean color $(V-K)_0 = 4.0$ mag of their LMC fields, the LMC zero point is -4.088 ± 0.011 mag.

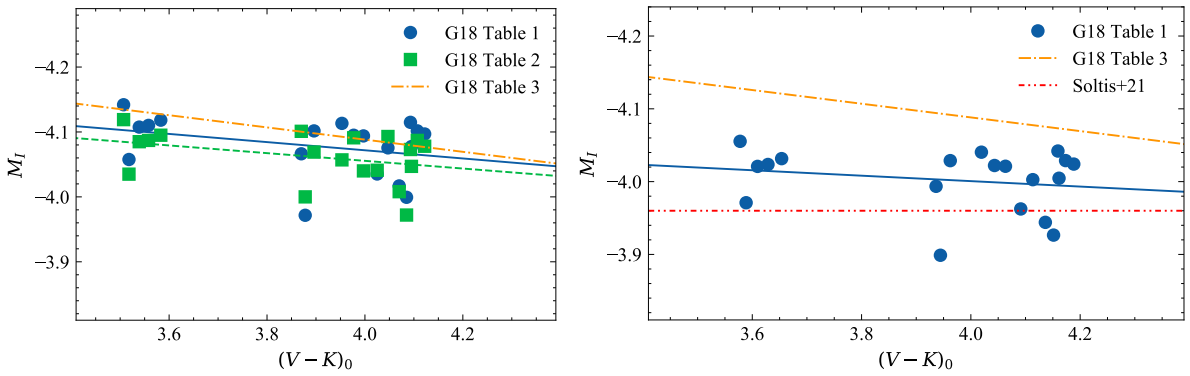

Figure 3.3: **Reproductions of the G18 results. a.** G18 results reproduced as originally quoted. The TRGB magnitudes from their Table 1, after applying their Table 2 corrections to an absolute system, are plotted (blue circles) with the best-fit line (solid blue line). Absolute magnitudes and colors from Table 2 (green squares) are plotted with a best-fit (dashed green line) line. The adopted calibration from G18 Table 3 is also shown (dot-dashed orange line). None of the three datasets were consistent with one another. **b.** Rescaling the absolutely calibrated G18 Table 1 measurements onto the OGLE-IV reddening zero point (blue points and line). The original G18 calibration is plotted for reference (dot-dashed orange line). Plotted is the TRGB calibration presented by Soltis et al.[56] that is meant to be made from this same dataset, where the authors did not control for metallicity/color (dashed red line).

As in the previous section, the G18 analysis is revisited at the photometry level to verify their TRGB measurements can be reproduced. To each of their adopted fields (5/40 available in the SMC and 14/116 available in the LMC), the apparent TRGB magnitude is determined. Good agreement is found with the G18 TRGB measurements presented in their Table 1, with an offset of $I^{TRGB} - I^{TRGB}_{G18} = +0.006 \pm 0.03$ mag when using an un-weighted Sobel kernel vs. -0.017 ± 0.028 mag when using the Poisson-weighted Sobel (the "PN" filter, following the nomenclature defined in G18). Thus, it is confirmed that both sets of methodologies are consistent in their TRGB measurements. A divergence is seen between the TRGB as measured via weighted and unweighted edge detection kernels. This is consistent with G18's findings and is explained by the low quality TRGB features contained in these fields that cause small changes in edge measurement methodology to produce significant shifts in the measured Tip magnitude. This is only a problem in the kinds of populations that were removed from this study's analysis.

After confirming the raw G18 measurements could be reproduced, it is sensible to now check for internal consistency between their Table 1 (apparent measured magnitudes), Table 2 (calibrated absolute magnitudes), and Table 3 (final adopted calibration). However, consistency between any of their three tables was not able to be established. The absolute magnitudes in their Table 2 (green squares in Figure 3.3a) could not be reproduced by combining the Table 1 apparent magnitudes, the tabulated reddenings and presented values of A_λ, the tabulated geometric corrections and their adopted DEB distance (blue circles in Figure 3.3a).[41] Furthermore, the calibration equation in their Table 3 (orange dot dashed line in Figure 3.3a,b) could not be reproduced from a fit to either the data in Table 1 (solid blue line in Figure 3.3a) or Table 2 (dashed green line in Figure 3.3a). The three sets of calibrations in order of Table 1 to 3 are:

$$\begin{aligned} M_I^{G18} &= -4.084(\pm 0.011) + 0.063(\pm 0.045)(V_0 - K_0 - 3.8) \\ &= -4.067(\pm 0.009) + 0.059(\pm 0.039)(V_0 - K_0 - 3.8) \\ &= -4.107(\pm 0.008) + 0.094(\pm 0.034)(V_0 - K_0 - 3.8) \end{aligned}$$

indicating the very steep slope and bright zero point of the TRGB as presented by G18 cannot be reproduced from their tables.

Indeed, the absolute magnitudes and dereddened colors in Table 2 are not the same values plotted in their Figures 6, 7, and 8 which were used to determine their calibration. For example, the brightest M_I value in their Table 2 is -4.119 mag, while the brightest M_I value in their Figures 6, 7, and 8 is close to -4.18 mag. The source of disagreement between the values quoted in their Table 2 and those plotted in Figures 6, 7, and 8 is not understood.

It was also not clear from where G18 derived their adopted ratios of selective to total absorption. In their paper it is stated that they used a "Schlegel et al. reddening law."[1]

1. Note that the reddening law adopted by SFD98 is a combination of the O'Donnell (1994) and the Cardelli, Clayton, and Mathis (1989) curves.

However, after direct inspection of SFD98 Table 6, the G18 adopted value of $A_V = 1.08R_V$ for $R_V = 3.1$ could not be confirmed, and the same is true for the rest of their adopted ratios of selective-to-total absorption.

3.3.2 Renormalization to Homogeneous Reddening and Distance Measurements

To enable accurate comparison with this study's calibrations, the magnitudes from G18 Table 1 and colors from G18 Table 2 are shifted by the differences between the later presented Gorski+20[18] reddening map and that from OGLE-IV ($\Delta E(V-I) = 0.048$ mag and 0.045 mag for the SMC and LMC, respectively).[55] The magnitudes are then calibrated by the updated DEB distances [42, 22] and a new fit is made to these renormalized datapoints (blue points and blue solid line in Figure 3.3b).

The best-fit line is $M_I^{G18'} = -4.008(\pm 0.012) + 0.037(\pm 0.045)(V_0 - K_0 - 3.8)$. Scaling the zero point to the mean LMC color of $(V-K)_0 = 4.1$ mag returns a value $M_I = -3.997 \pm 0.018$ mag, which is entered into Table 1.4 under the Renormalized column. By simply updating to modern DEB distances and to the S21 reddening map, the slope is considerably flattened as compared to that originally adopted by G18 (orange dot-dashed line in Figure 3.3).

Soltis et al.[56] quoted an $M_I = -3.96 \pm 0.011$ mag using these same measurements presented in G18 (red dot-dot-dashed line in Figure 3.3b). However, they took a simple average of the raw G18 magnitudes and did not account for color/metallicity effects, which was a primary goal of the original G18 study. As a result, their quoted calibration is biased to fainter magnitudes by ~ 0.04 mag, in addition to the similarly-sized bimodality bias discussed in the main text and in Figure 1.13.

3.4 F20

3.4.1 Original Study

F20 presented a calibration of the TRGB zero point using a differential, multi-wavelength technique that simultaneously constrained the distances and reddenings to TRGB stars. F20 detailed the sample they used to perform their LMC analysis, despite claims made to the contrary in the recent literature.[36, 56] Directly following their Sections 3 and 3.2, the entire OGLE-III (in their case OGLE-III Shallow) footprint, minus the inner 1 deg, is adopted for the reanalysis undertaken in this section.

3.4.2 Renormalization to Homogeneous Reddening and Distance Measurements

To compute the F20 renormalized result, a scalar offset in M_I is determined from the difference between the mean of the OGLE-IV reddening map over the entire F20 sample ($E(V-I) = 0.113$ mag) and the F20 reddening determination ($E(V-I) = 0.136$ mag) which gives $M_I = -4.018$ mag.

3.4.3 On the F20 SMC Calibration

F20 also presented a separate TRGB zero point calibration using the SMC with the SFD98/SF11 foreground estimate of $A_I = 0.056$, an earlier DEB distance[20], and an apparent TRGB measurement $I = 14.93$ mag to determine an $M_I = -4.09 \pm 0.03_{stat} \pm 0.05_{sys}$ mag. However, given the agreement of their quoted apparent TRGB measurement with this study's extinction-corrected measurement, it is likely that the TRGB magnitude quoted as *apparent* by F20 had already been corrected for foreground extinction, i.e., the reddening correction may have been twice-applied. This is corroborated in a follow-up discussion in Freedman21.[11] Adopting instead 14.93 as the extinction-corrected TRGB, their SMC de-

termination becomes $-4.035 \pm 0.03_{stat} \pm 0.05_{sys}$ mag, which is in very good agreement with the measurements of this study.

As a check, the apparent TRGB magnitude is measured from the SMC using the same error estimation methodology of this study and determined to be $I = 14.99 \pm 0.03$ mag. Adopting the updated G20 DEB distance, and again the SFD98/SF11 foreground estimate, gives $M_I = -4.040 \pm 0.04_{stat} \pm 0.03_{sys}$ mag. This value is in very good agreement with that determined in this study.

REFERENCES

[1] Gagandeep S. Anand, Luca Rizzi, R. Brent Tully, Edward J. Shaya, Igor D. Karachentsev, Dmitry I. Makarov, Lidia Makarova, Po-Feng Wu, Andrew E. Dolphin, and Ehsan Kourkchi. The Extragalactic Distance Database: The Color-Magnitude Diagrams and Tip of the Red Giant Branch Distances Catalog. *arXiv e-prints*, art. arXiv:2104.02649, April 2021.

[2] Michele Bellazzini, Francesco R. Ferraro, and Elena Pancino. A Step toward the Calibration of the Red Giant Branch Tip as a Standard Candle. *The Astrophysical Journal*, 556(2):635–640, August 2001. doi:10.1086/321613.

[3] M. Cappellari and Y. Copin. Adaptive spatial binning of integral-field spectroscopic data using Voronoi tessellations. *MNRAS*, 342:345–354, June 2003. doi:10.1046/j.1365-8711.2003.06541.x.

[4] Yumi Choi, David L. Nidever, Knut Olsen, Gurtina Besla, Robert D. Blum, Dennis Zaritsky, Maria-Rosa L. Cioni, Roeland P. van der Marel, Eric F. Bell, L. Clifton Johnson, A. Katherina Vivas, Alistair R. Walker, Thomas J. L. de Boer, Noelia E. D. Noël, Antonela Monachesi, Carme Gallart, Matteo Monelli, Guy S. Stringfellow, Pol Massana, David Martinez-Delgado, and Ricardo R. Muñoz. SMASHing the LMC: Mapping a Ring-like Stellar Overdensity in the LMC Disk. *The Astrophysical Journal*, 869(2): 125, December 2018. doi:10.3847/1538-4357/aaed1f.

[5] M. R. L. Cioni, H. J. Habing, and F. P. Israel. The morphology of the Magellanic Clouds revealed by stars of different age: results from the DENIS survey. *Astronomy and Astrophysics*, 358:L9–L12, June 2000.

[6] F. Cusano, M. I. Moretti, G. Clementini, V. Ripepi, M. Marconi, M. R. L. Cioni, S. Rubele, A. Garofalo, R. de Grijs, M. A. T. Groenewegen, J. M. Oliveira, S. Subramanian, N. C. Sun, and J. Th. van Loon. The VMC Survey – XLII. Near-infrared period-luminosity relations for RR Lyrae stars and the structure of the Large Magellanic Cloud. *arXiv e-prints*, art. arXiv:2103.15492, March 2021.

[7] G. S. Da Costa and T. E. Armandroff. Standard Globular Cluster Giant Branches in the (M(I), (V - I)o) Plane. *The Astronomical Journal*, 100:162, July 1990. doi:10.1086/115500.

[8] G. de Vaucouleurs and K. C. Freeman. Structure and dynamics of barred spiral galaxies, in particular of the Magellanic type. *Vistas in Astronomy*, 14(1):163–294, January 1972. doi:10.1016/0083-6656(72)90026-8.

[9] C. Fabricius, X. Luri, F. Arenou, C. Babusiaux, A. Helmi, T. Muraveva, C. Reylé, F. Spoto, A. Vallenari, T. Antoja, E. Balbinot, C. Barache, N. Bauchet, A. Bragaglia, D. Busonero, T. Cantat-Gaudin, J. M. Carrasco, S. Diakité, M. Fabrizio, F. Figueras, A. Garcia-Gutierrez, A. Garofalo, C. Jordi, P. Kervella, S. Khanna, N. Leclerc, E. Licata,

S. Lambert, P. M. Marrese, A. Masip, P. Ramos, N. Robichon, A. C. Robin, M. Romero-Gómez, S. Rubele, and M. Weiler. Gaia Early Data Release 3. Catalogue validation. *Astronomy and Astrophysics*, 649:A5, May 2021. doi:10.1051/0004-6361/202039834.

[10] Edward L. Fitzpatrick. Correcting for the Effects of Interstellar Extinction. *Publications of the Astronomical Society of the Pacific*, 111(755):63–75, January 1999. doi:10.1086/316293.

[11] Wendy L. Freedman. Measurements of the Hubble Constant: Tensions in Perspective. *The Astrophysical Journal*, 919(1):16, September 2021. doi:10.3847/1538-4357/ac0e95.

[12] Wendy L. Freedman, Barry F. Madore, Dylan Hatt, Taylor J. Hoyt, In Sung Jang, Rachael L. Beaton, Christopher R. Burns, Myung Gyoon Lee, Andrew J. Monson, Jillian R. Neeley, M. M. Phillips, Jeffrey A. Rich, and Mark Seibert. The Carnegie-Chicago Hubble Program. VIII. An Independent Determination of the Hubble Constant Based on the Tip of the Red Giant Branch. *The Astrophysical Journal*, 882(1):34, September 2019. doi:10.3847/1538-4357/ab2f73.

[13] Wendy L. Freedman, Barry F. Madore, Taylor Hoyt, In Sung Jang, Rachael Beaton, Myung Gyoon Lee, Andrew Monson, Jill Neeley, and Jeffrey Rich. Calibration of the Tip of the Red Giant Branch. *The Astrophysical Journal*, 891(1):57, March 2020. doi:10.3847/1538-4357/ab7339.

[14] Gaia Collaboration, T. Prusti, J. H. J. de Bruijne, A. G. A. Brown, A. Vallenari, C. Babusiaux, C. A. L. Bailer-Jones, U. Bastian, M. Biermann, D. W. Evans, L. Eyer, F. Jansen, C. Jordi, S. A. Klioner, U. Lammers, L. Lindegren, X. Luri, F. Mignard, D. J. Milligan, C. Panem, V. Poinsignon, D. Pourbaix, S. Randich, G. Sarri, P. Sartoretti, H. I. Siddiqui, C. Soubiran, V. Valette, F. van Leeuwen, N. A. Walton, C. Aerts, F. Arenou, M. Cropper, R. Drimmel, E. Høg, D. Katz, M. G. Lattanzi, W. O'Mullane, E. K. Grebel, A. D. Holland, C. Huc, X. Passot, L. Bramante, C. Cacciari, J. Castañeda, L. Chaoul, N. Cheek, F. De Angeli, C. Fabricius, R. Guerra, J. Hernández, A. Jean-Antoine-Piccolo, E. Masana, R. Messineo, N. Mowlavi, K. Nienartowicz, D. Ordóñez-Blanco, P. Panuzzo, J. Portell, P. J. Richards, M. Riello, G. M. Seabroke, P. Tanga, F. Thévenin, J. Torra, S. G. Els, G. Gracia-Abril, G. Comoretto, M. Garcia-Reinaldos, T. Lock, E. Mercier, M. Altmann, R. Andrae, T. L. Astraatmadja, I. Bellas-Velidis, K. Benson, J. Berthier, R. Blomme, G. Busso, B. Carry, A. Cellino, G. Clementini, S. Cowell, O. Creevey, J. Cuypers, M. Davidson, J. De Ridder, A. de Torres, L. Delchambre, A. Dell'Oro, C. Ducourant, Y. Frémat, M. García-Torres, E. Gosset, J. L. Halbwachs, N. C. Hambly, D. L. Harrison, M. Hauser, D. Hestroffer, S. T. Hodgkin, H. E. Huckle, A. Hutton, G. Jasniewicz, S. Jordan, M. Kontizas, A. J. Korn, A. C. Lanzafame, M. Manteiga, A. Moitinho, K. Muinonen, J. Osinde, E. Pancino, T. Pauwels, J. M. Petit, A. Recio-Blanco, A. C. Robin, L. M. Sarro, C. Siopis, M. Smith, K. W. Smith, A. Sozzetti, W. Thuillot, W. van Reeven, Y. Viala, U. Abbas, A. Abreu Aramburu, S. Accart, J. J. Aguado, P. M. Allan, W. Allasia, G. Altavilla, M. A. Álvarez, J. Alves, R. I. Anderson, A. H. Andrei, E. Anglada Varela, E. Antiche, T. Antoja, S. Antón,

B. Arcay, A. Atzei, L. Ayache, N. Bach, S. G. Baker, L. Balaguer-Núñez, C. Barache, C. Barata, A. Barbier, F. Barblan, M. Baroni, D. Barrado y Navascués, M. Barros, M. A. Barstow, U. Becciani, M. Bellazzini, G. Bellei, A. Bello García, V. Belokurov, P. Bendjoya, A. Berihuete, L. Bianchi, O. Bienaymé, F. Billebaud, N. Blagorodnova, S. Blanco-Cuaresma, T. Boch, A. Bombrun, R. Borrachero, S. Bouquillon, G. Bourda, H. Bouy, A. Bragaglia, M. A. Breddels, N. Brouillet, T. Brüsemeister, B. Bucciarelli, F. Budnik, P. Burgess, R. Burgon, A. Burlacu, D. Busonero, R. Buzzi, E. Caffau, J. Cambras, H. Campbell, R. Cancelliere, T. Cantat-Gaudin, T. Carlucci, J. M. Carrasco, M. Castellani, P. Charlot, J. Charnas, P. Charvet, F. Chassat, A. Chiavassa, M. Clotet, G. Cocozza, R. S. Collins, P. Collins, G. Costigan, F. Crifo, N. J. G. Cross, M. Crosta, C. Crowley, C. Dafonte, Y. Damerdji, A. Dapergolas, P. David, M. David, P. De Cat, F. de Felice, P. de Laverny, F. De Luise, R. De March, D. de Martino, R. de Souza, J. Debosscher, E. del Pozo, M. Delbo, A. Delgado, H. E. Delgado, F. di Marco, P. Di Matteo, S. Diakite, E. Distefano, C. Dolding, S. Dos Anjos, P. Drazinos, J. Durán, Y. Dzigan, E. Ecale, B. Edvardsson, H. Enke, M. Erdmann, D. Escolar, M. Espina, N. W. Evans, G. Eynard Bontemps, C. Fabre, M. Fabrizio, S. Faigler, A. J. Falcão, M. Farràs Casas, F. Faye, L. Federici, G. Fedorets, J. Fernández-Hernández, P. Fernique, A. Fienga, F. Figueras, F. Filippi, K. Findeisen, A. Fonti, M. Fouesneau, E. Fraile, M. Fraser, J. Fuchs, R. Furnell, M. Gai, S. Galleti, L. Galluccio, D. Garabato, F. García-Sedano, P. Garé, A. Garofalo, N. Garralda, P. Gavras, J. Gerssen, R. Geyer, G. Gilmore, S. Girona, G. Giuffrida, M. Gomes, A. González-Marcos, J. González-Núñez, J. J. González-Vidal, M. Granvik, A. Guerrier, P. Guillout, J. Guiraud, A. Gúrpide, R. Gutiérrez-Sánchez, L. P. Guy, R. Haigron, D. Hatzidimitriou, M. Haywood, U. Heiter, A. Helmi, D. Hobbs, W. Hofmann, B. Holl, G. Holland, J. A. S. Hunt, A. Hypki, V. Icardi, M. Irwin, G. Jevardat de Fombelle, P. Jofré, P. G. Jonker, A. Jorissen, F. Julbe, A. Karampelas, A. Kochoska, R. Kohley, K. Kolenberg, E. Kontizas, S. E. Koposov, G. Kordopatis, P. Koubsky, A. Kowalczyk, A. Krone-Martins, M. Kudryashova, I. Kull, R. K. Bachchan, F. Lacoste-Seris, A. F. Lanza, J. B. Lavigne, C. Le Poncin-Lafitte, Y. Lebreton, T. Lebzelter, S. Leccia, N. Leclerc, I. Lecoeur-Taibi, V. Lemaitre, H. Lenhardt, F. Leroux, S. Liao, E. Licata, H. E. P. Lindstrøm, T. A. Lister, E. Livanou, A. Lobel, W. Löffler, M. López, A. Lopez-Lozano, D. Lorenz, T. Loureiro, I. MacDonald, T. Magalhães Fernandes, S. Managau, R. G. Mann, G. Mantelet, O. Marchal, J. M. Marchant, M. Marconi, J. Marie, S. Marinoni, P. M. Marrese, G. Marschalkó, D. J. Marshall, J. M. Martín-Fleitas, M. Martino, N. Mary, G. Matijevič, T. Mazeh, P. J. McMillan, S. Messina, A. Mestre, D. Michalik, N. R. Millar, B. M. H. Miranda, D. Molina, R. Molinaro, M. Molinaro, L. Molnár, M. Moniez, P. Montegriffo, D. Monteiro, R. Mor, A. Mora, R. Morbidelli, T. Morel, S. Morgenthaler, T. Morley, D. Morris, A. F. Mulone, T. Muraveva, I. Musella, J. Narbonne, G. Nelemans, L. Nicastro, L. Noval, C. Ordénovic, J. Ordieres-Meré, P. Osborne, C. Pagani, I. Pagano, F. Pailler, H. Palacin, L. Palaversa, P. Parsons, T. Paulsen, M. Pecoraro, R. Pedrosa, H. Pentikäinen, J. Pereira, B. Pichon, A. M. Piersimoni, F. X. Pineau, E. Plachy, G. Plum, E. Poujoulet, A. Prša, L. Pulone, S. Ragaini, S. Rago, N. Rambaux, M. Ramos-Lerate, P. Ranalli, G. Rauw, A. Read, S. Regibo, F. Renk, C. Reylé, R. A. Ribeiro, L. Ri-

moldini, V. Ripepi, A. Riva, G. Rixon, M. Roelens, M. Romero-Gómez, N. Rowell, F. Royer, A. Rudolph, L. Ruiz-Dern, G. Sadowski, T. Sagristà Sellés, J. Sahlmann, J. Salgado, E. Salguero, M. Sarasso, H. Savietto, A. Schnorhk, M. Schultheis, E. Sciacca, M. Segol, J. C. Segovia, D. Segransan, E. Serpell, I. C. Shih, R. Smareglia, R. L. Smart, C. Smith, E. Solano, F. Solitro, R. Sordo, S. Soria Nieto, J. Souchay, A. Spagna, F. Spoto, U. Stampa, I. A. Steele, H. Steidelmüller, C. A. Stephenson, H. Stoev, F. F. Suess, M. Süveges, J. Surdej, L. Szabados, E. Szegedi-Elek, D. Tapiador, F. Taris, G. Tauran, M. B. Taylor, R. Teixeira, D. Terrett, B. Tingley, S. C. Trager, C. Turon, A. Ulla, E. Utrilla, G. Valentini, A. van Elteren, E. Van Hemelryck, M. van Leeuwen, M. Varadi, A. Vecchiato, J. Veljanoski, T. Via, D. Vicente, S. Vogt, H. Voss, V. Votruba, S. Voutsinas, G. Walmsley, M. Weiler, K. Weingrill, D. Werner, T. Wevers, G. Whitehead, Ł. Wyrzykowski, A. Yoldas, M. Žerjal, S. Zucker, C. Zurbach, T. Zwitter, A. Alecu, M. Allen, C. Allende Prieto, A. Amorim, G. Anglada-Escudé, V. Arsenijevic, S. Azaz, P. Balm, M. Beck, H. H. Bernstein, L. Bigot, A. Bijaoui, C. Blasco, M. Bonfigli, G. Bono, S. Boudreault, A. Bressan, S. Brown, P. M. Brunet, P. Bunclark, R. Buonanno, A. G. Butkevich, C. Carret, C. Carrion, L. Chemin, F. Chéreau, L. Corcione, E. Darmigny, K. S. de Boer, P. de Teodoro, P. T. de Zeeuw, C. Delle Luche, C. D. Domingues, P. Dubath, F. Fodor, B. Frézouls, A. Fries, D. Fustes, D. Fyfe, E. Gallardo, J. Gallegos, D. Gardiol, M. Gebran, A. Gomboc, A. Gómez, E. Grux, A. Gueguen, A. Heyrovsky, J. Hoar, G. Iannicola, Y. Isasi Parache, A. M. Janotto, E. Joliet, A. Jonckheere, R. Keil, D. W. Kim, P. Klagyivik, J. Klar, J. Knude, O. Kochukhov, I. Kolka, J. Kos, A. Kutka, V. Lainey, D. LeBouquin, C. Liu, D. Loreggia, V. V. Makarov, M. G. Marseille, C. Martayan, O. Martinez-Rubi, B. Massart, F. Meynadier, S. Mignot, U. Munari, A. T. Nguyen, T. Nordlander, P. Ocvirk, K. S. O'Flaherty, A. Olias Sanz, P. Ortiz, J. Osorio, D. Oszkiewicz, A. Ouzounis, M. Palmer, P. Park, E. Pasquato, C. Peltzer, J. Peralta, F. Péturaud, T. Pieniluoma, E. Pigozzi, J. Poels, G. Prat, T. Prod'homme, F. Raison, J. M. Rebordao, D. Risquez, B. Rocca-Volmerange, S. Rosen, M. I. Ruiz-Fuertes, F. Russo, S. Sembay, I. Serraller Vizcaino, A. Short, A. Siebert, H. Silva, D. Sinachopoulos, E. Slezak, M. Soffel, D. Sosnowska, V. Straižys, M. ter Linden, D. Terrell, S. Theil, C. Tiede, L. Troisi, P. Tsalmantza, D. Tur, M. Vaccari, F. Vachier, P. Valles, W. Van Hamme, L. Veltz, J. Virtanen, J. M. Wallut, R. Wichmann, M. I. Wilkinson, H. Ziaeepour, and S. Zschocke. The Gaia mission. *Astronomy and Astrophysics*, 595: A1, November 2016. doi:10.1051/0004-6361/201629272.

[15] Gaia Collaboration, A. G. A. Brown, A. Vallenari, T. Prusti, J. H. J. de Bruijne, C. Babusiaux, M. Biermann, O. L. Creevey, D. W. Evans, L. Eyer, A. Hutton, F. Jansen, C. Jordi, S. A. Klioner, U. Lammers, L. Lindegren, X. Luri, F. Mignard, C. Panem, D. Pourbaix, S. Randich, P. Sartoretti, C. Soubiran, N. A. Walton, F. Arenou, C. A. L. Bailer-Jones, U. Bastian, M. Cropper, R. Drimmel, D. Katz, M. G. Lattanzi, F. van Leeuwen, J. Bakker, C. Cacciari, J. Castañeda, F. De Angeli, C. Ducourant, C. Fabricius, M. Fouesneau, Y. Frémat, R. Guerra, A. Guerrier, J. Guiraud, A. Jean-Antoine Piccolo, E. Masana, R. Messineo, N. Mowlavi, C. Nicolas, K. Nienartowicz, F. Pailler, P. Panuzzo, F. Riclet, W. Roux, G. M. Seabroke, R. Sordo, P. Tanga, F. Thévenin, G. Gracia-Abril, J. Portell, D. Teyssier, M. Altmann, R. Andrae, I. Bellas-

Velidis, K. Benson, J. Berthier, R. Blomme, E. Brugaletta, P. W. Burgess, G. Busso, B. Carry, A. Cellino, N. Cheek, G. Clementini, Y. Damerdji, M. Davidson, L. Delchambre, A. Dell'Oro, J. Fernández-Hernández, L. Galluccio, P. García-Lario, M. Garcia-Reinaldos, J. González-Núñez, E. Gosset, R. Haigron, J. L. Halbwachs, N. C. Hambly, D. L. Harrison, D. Hatzidimitriou, U. Heiter, J. Hernández, D. Hestroffer, S. T. Hodgkin, B. Holl, K. Janßen, G. Jevardat de Fombelle, S. Jordan, A. Krone-Martins, A. C. Lanzafame, W. Löffler, A. Lorca, M. Manteiga, O. Marchal, P. M. Marrese, A. Moitinho, A. Mora, K. Muinonen, P. Osborne, E. Pancino, T. Pauwels, J. M. Petit, A. Recio-Blanco, P. J. Richards, M. Riello, L. Rimoldini, A. C. Robin, T. Roegiers, J. Rybizki, L. M. Sarro, C. Siopis, M. Smith, A. Sozzetti, A. Ulla, E. Utrilla, M. van Leeuwen, W. van Reeven, U. Abbas, A. Abreu Aramburu, S. Accart, C. Aerts, J. J. Aguado, M. Ajaj, G. Altavilla, M. A. Álvarez, J. Álvarez Cid-Fuentes, J. Alves, R. I. Anderson, E. Anglada Varela, T. Antoja, M. Audard, D. Baines, S. G. Baker, L. Balaguer-Núñez, E. Balbinot, Z. Balog, C. Barache, D. Barbato, M. Barros, M. A. Barstow, S. Bartolomé, J. L. Bassilana, N. Bauchet, A. Baudesson-Stella, U. Becciani, M. Bellazzini, M. Bernet, S. Bertone, L. Bianchi, S. Blanco-Cuaresma, T. Boch, A. Bombrun, D. Bossini, S. Bouquillon, A. Bragaglia, L. Bramante, E. Breedt, A. Bressan, N. Brouillet, B. Bucciarelli, A. Burlacu, D. Busonero, A. G. Butkevich, R. Buzzi, E. Caffau, R. Cancelliere, H. Cánovas, T. Cantat-Gaudin, R. Carballo, T. Carlucci, M. I. Carnerero, J. M. Carrasco, L. Casamiquela, M. Castellani, A. Castro-Ginard, P. Castro Sampol, L. Chaoul, P. Charlot, L. Chemin, A. Chiavassa, M. R. L. Cioni, G. Comoretto, W. J. Cooper, T. Cornez, S. Cowell, F. Crifo, M. Crosta, C. Crowley, C. Dafonte, A. Dapergolas, M. David, P. David, P. de Laverny, F. De Luise, R. De March, J. De Ridder, R. de Souza, P. de Teodoro, A. de Torres, E. F. del Peloso, E. del Pozo, M. Delbo, A. Delgado, H. E. Delgado, J. B. Delisle, P. Di Matteo, S. Diakite, C. Diener, E. Distefano, C. Dolding, D. Eappachen, B. Edvardsson, H. Enke, P. Esquej, C. Fabre, M. Fabrizio, S. Faigler, G. Fedorets, P. Fernique, A. Fienga, F. Figueras, C. Fouron, F. Fragkoudi, E. Fraile, F. Franke, M. Gai, D. Garabato, A. Garcia-Gutierrez, M. García-Torres, A. Garofalo, P. Gavras, E. Gerlach, R. Geyer, P. Giacobbe, G. Gilmore, S. Girona, G. Giuffrida, R. Gomel, A. Gomez, I. Gonzalez-Santamaria, J. J. González-Vidal, M. Granvik, R. Gutiérrez-Sánchez, L. P. Guy, M. Hauser, M. Haywood, A. Helmi, S. L. Hidalgo, T. Hilger, N. Hładczuk, D. Hobbs, G. Holland, H. E. Huckle, G. Jasniewicz, P. G. Jonker, J. Juaristi Campillo, F. Julbe, L. Karbevska, P. Kervella, S. Khanna, A. Kochoska, M. Kontizas, G. Kordopatis, A. J. Korn, Z. Kostrzewa-Rutkowska, K. Kruszyńska, S. Lambert, A. F. Lanza, Y. Lasne, J. F. Le Campion, Y. Le Fustec, Y. Lebreton, T. Lebzelter, S. Leccia, N. Leclerc, I. Lecoeur-Taibi, S. Liao, E. Licata, E. P. Lindstrøm, T. A. Lister, E. Livanou, A. Lobel, P. Madrero Pardo, S. Managau, R. G. Mann, J. M. Marchant, M. Marconi, M. M. S. Marcos Santos, S. Marinoni, F. Marocco, D. J. Marshall, L. Martin Polo, J. M. Martín-Fleitas, A. Masip, D. Massari, A. Mastrobuono-Battisti, T. Mazeh, P. J. McMillan, S. Messina, D. Michalik, N. R. Millar, A. Mints, D. Molina, R. Molinaro, L. Molnár, P. Montegriffo, R. Mor, R. Morbidelli, T. Morel, D. Morris, A. F. Mulone, D. Munoz, T. Muraveva, C. P. Murphy, I. Musella, L. Noval, C. Ordénovic, G. Orrù, J. Osinde, C. Pagani, I. Pagano, L. Palaversa, P. A. Pali-

cio, A. Panahi, M. Pawlak, X. Peñalosa Esteller, A. Penttilä, A. M. Piersimoni, F. X. Pineau, E. Plachy, G. Plum, E. Poggio, E. Poretti, E. Poujoulet, A. Prša, L. Pulone, E. Racero, S. Ragaini, M. Rainer, C. M. Raiteri, N. Rambaux, P. Ramos, M. Ramos-Lerate, P. Re Fiorentin, S. Regibo, C. Reylé, V. Ripepi, A. Riva, G. Rixon, N. Robichon, C. Robin, M. Roelens, L. Rohrbasser, M. Romero-Gómez, N. Rowell, F. Royer, K. A. Rybicki, G. Sadowski, A. Sagristà Sellés, J. Sahlmann, J. Salgado, E. Salguero, N. Samaras, V. Sanchez Gimenez, N. Sanna, R. Santoveña, M. Sarasso, M. Schultheis, E. Sciacca, M. Segol, J. C. Segovia, D. Ségransan, D. Semeux, S. Shahaf, H. I. Siddiqui, A. Siebert, L. Siltala, E. Slezak, R. L. Smart, E. Solano, F. Solitro, D. Souami, J. Souchay, A. Spagna, F. Spoto, I. A. Steele, H. Steidelmüller, C. A. Stephenson, M. Süveges, L. Szabados, E. Szegedi-Elek, F. Taris, G. Tauran, M. B. Taylor, R. Teixeira, W. Thuillot, N. Tonello, F. Torra, J. Torra, C. Turon, N. Unger, M. Vaillant, E. van Dillen, O. Vanel, A. Vecchiato, Y. Viala, D. Vicente, S. Voutsinas, M. Weiler, T. Wevers, Ł. Wyrzykowski, A. Yoldas, P. Yvard, H. Zhao, J. Zorec, S. Zucker, C. Zurbach, and T. Zwitter. Gaia Early Data Release 3. Summary of the contents and survey properties. *Astronomy and Astrophysics*, 649:A1, May 2021. doi:10.1051/0004-6361/202039657.

[16] Gaia Collaboration, X. Luri, L. Chemin, G. Clementini, H. E. Delgado, P. J. McMillan, M. Romero-Gómez, E. Balbinot, A. Castro-Ginard, R. Mor, V. Ripepi, L. M. Sarro, M. R. L. Cioni, C. Fabricius, A. Garofalo, A. Helmi, T. Muraveva, A. G. A. Brown, A. Vallenari, T. Prusti, J. H. J. de Bruijne, C. Babusiaux, M. Biermann, O. L. Creevey, D. W. Evans, L. Eyer, A. Hutton, F. Jansen, C. Jordi, S. A. Klioner, U. Lammers, L. Lindegren, F. Mignard, C. Panem, D. Pourbaix, S. Randich, P. Sartoretti, C. Soubiran, N. A. Walton, F. Arenou, C. A. L. Bailer-Jones, U. Bastian, M. Cropper, R. Drimmel, D. Katz, M. G. Lattanzi, F. van Leeuwen, J. Bakker, J. Castañeda, F. De Angeli, C. Ducourant, M. Fouesneau, Y. Frémat, R. Guerra, A. Guerrier, J. Guiraud, A. Jean-Antoine Piccolo, E. Masana, R. Messineo, N. Mowlavi, C. Nicolas, K. Nienartowicz, F. Pailler, P. Panuzzo, F. Riclet, W. Roux, G. M. Seabroke, R. Sordo, P. Tanga, F. Thévenin, G. Gracia-Abril, J. Portell, D. Teyssier, M. Altmann, R. Andrae, I. Bellas-Velidis, K. Benson, J. Berthier, R. Blomme, E. Brugaletta, P. W. Burgess, G. Busso, B. Carry, A. Cellino, N. Cheek, Y. Damerdji, M. Davidson, L. Delchambre, A. Dell'Oro, J. Fernández-Hernández, L. Galluccio, P. García-Lario, M. Garcia-Reinaldos, J. González-Núñez, E. Gosset, R. Haigron, J. L. Halbwachs, N. C. Hambly, D. L. Harrison, D. Hatzidimitriou, U. Heiter, J. Hernández, D. Hestroffer, S. T. Hodgkin, B. Holl, K. Janßen, G. Jevardat de Fombelle, S. Jordan, A. Krone-Martins, A. C. Lanzafame, W. Löffler, A. Lorca, M. Manteiga, O. Marchal, P. M. Marrese, A. Moitinho, A. Mora, K. Muinonen, P. Osborne, E. Pancino, T. Pauwels, A. Recio-Blanco, P. J. Richards, M. Riello, L. Rimoldini, A. C. Robin, T. Roegiers, J. Rybizki, C. Siopis, M. Smith, A. Sozzetti, A. Ulla, E. Utrilla, M. van Leeuwen, W. van Reeven, U. Abbas, A. Abreu Aramburu, S. Accart, C. Aerts, J. J. Aguado, M. Ajaj, G. Altavilla, M. A. Álvarez, J. Álvarez Cid-Fuentes, J. Alves, R. I. Anderson, E. Anglada Varela, T. Antoja, M. Audard, D. Baines, S. G. Baker, L. Balaguer-Núñez, Z. Balog, C. Barache, D. Barbato, M. Barros, M. A. Barstow, S. Bartolomé, J. L. Bassilana, N. Bauchet, A. Baudesson-Stella, U. Becciani, M. Bellazzini, M. Ber-

net, S. Bertone, L. Bianchi, S. Blanco-Cuaresma, T. Boch, A. Bombrun, D. Bossini, S. Bouquillon, A. Bragaglia, L. Bramante, E. Breedt, A. Bressan, N. Brouillet, B. Bucciarelli, A. Burlacu, D. Busonero, A. G. Butkevich, R. Buzzi, E. Caffau, R. Cancelliere, H. Cánovas, T. Cantat-Gaudin, R. Carballo, T. Carlucci, M. I. Carnerero, J. M. Carrasco, L. Casamiquela, M. Castellani, P. Castro Sampol, L. Chaoul, P. Charlot, A. Chiavassa, G. Comoretto, W. J. Cooper, T. Cornez, S. Cowell, F. Crifo, M. Crosta, C. Crowley, C. Dafonte, A. Dapergolas, M. David, P. David, P. de Laverny, F. De Luise, R. De March, J. De Ridder, R. de Souza, P. de Teodoro, A. de Torres, E. F. del Peloso, E. del Pozo, A. Delgado, J. B. Delisle, P. Di Matteo, S. Diakite, C. Diener, E. Distefano, C. Dolding, D. Eappachen, H. Enke, P. Esquej, C. Fabre, M. Fabrizio, S. Faigler, G. Fedorets, P. Fernique, A. Fienga, F. Figueras, C. Fouron, F. Fragkoudi, E. Fraile, F. Franke, M. Gai, D. Garabato, A. Garcia-Gutierrez, M. García-Torres, P. Gavras, E. Gerlach, R. Geyer, P. Giacobbe, G. Gilmore, S. Girona, G. Giuffrida, A. Gomez, I. Gonzalez-Santamaria, J. J. González-Vidal, M. Granvik, R. Gutiérrez-Sánchez, L. P. Guy, M. Hauser, M. Haywood, S. L. Hidalgo, T. Hilger, N. Hładczuk, D. Hobbs, G. Holland, H. E. Huckle, G. Jasniewicz, P. G. Jonker, J. Juaristi Campillo, F. Julbe, L. Karbevska, P. Kervella, S. Khanna, A. Kochoska, M. Kontizas, G. Kordopatis, A. J. Korn, Z. Kostrzewa-Rutkowska, K. Kruszyńska, S. Lambert, A. F. Lanza, Y. Lasne, J. F. Le Campion, Y. Le Fustec, Y. Lebreton, T. Lebzelter, S. Leccia, N. Leclerc, I. Lecoeur-Taibi, S. Liao, E. Licata, H. E. P. Lindstrøm, T. A. Lister, E. Livanou, A. Lobel, P. Madrero Pardo, S. Managau, R. G. Mann, J. M. Marchant, M. Marconi, M. M. S. Marcos Santos, S. Marinoni, F. Marocco, D. J. Marshall, L. Martin Polo, J. M. Martín-Fleitas, A. Masip, D. Massari, A. Mastrobuono-Battisti, T. Mazeh, S. Messina, D. Michalik, N. R. Millar, A. Mints, D. Molina, R. Molinaro, L. Molnár, P. Montegriffo, R. Morbidelli, T. Morel, D. Morris, A. F. Mulone, D. Munoz, C. P. Murphy, I. Musella, L. Noval, C. Ordénovic, G. Orrù, J. Osinde, C. Pagani, I. Pagano, L. Palaversa, P. A. Palicio, A. Panahi, M. Pawlak, X. Peñalosa Esteller, A. Penttilä, A. M. Piersimoni, F. X. Pineau, E. Plachy, G. Plum, E. Poggio, E. Poretti, E. Poujoulet, A. Prša, L. Pulone, E. Racero, S. Ragaini, M. Rainer, C. M. Raiteri, N. Rambaux, P. Ramos, M. Ramos-Lerate, P. Re Fiorentin, S. Regibo, C. Reylé, A. Riva, G. Rixon, N. Robichon, C. Robin, M. Roelens, L. Rohrbasser, N. Rowell, F. Royer, K. A. Rybicki, G. Sadowski, A. Sagristà Sellés, J. Sahlmann, J. Salgado, E. Salguero, N. Samaras, V. Sanchez Gimenez, N. Sanna, R. Santoveña, M. Sarasso, M. Schultheis, E. Sciacca, M. Segol, J. C. Segovia, D. Ségransan, D. Semeux, H. I. Siddiqui, A. Siebert, L. Siltala, E. Slezak, R. L. Smart, E. Solano, F. Solitro, D. Souami, J. Souchay, A. Spagna, F. Spoto, I. A. Steele, H. Steidelmüller, C. A. Stephenson, M. Süveges, L. Szabados, E. Szegedi-Elek, F. Taris, G. Tauran, M. B. Taylor, R. Teixeira, W. Thuillot, N. Tonello, F. Torra, J. Torra, C. Turon, N. Unger, M. Vaillant, E. van Dillen, O. Vanel, A. Vecchiato, Y. Viala, D. Vicente, S. Voutsinas, M. Weiler, T. Wevers, Ł. Wyrzykowski, A. Yoldas, P. Yvard, H. Zhao, J. Zorec, S. Zucker, C. Zurbach, and T. Zwitter. Gaia Early Data Release 3. Structure and properties of the Magellanic Clouds. *Astronomy and Astrophysics*, 649:A7, May 2021. doi:10.1051/0004-6361/202039588.

[17] Marek Górski, Grzegorz Pietrzyński, Wolfgang Gieren, Dariusz Graczyk, Ksenia Su-

chomska, Paulina Karczmarek, Roger E. Cohen, Bartłomiej Zgirski, Piotr Wielgórski, Bogumił Pilecki, Mónica Taormina, Zbigniew Kołaczkowski, and Weronika Narloch. The araucaria project: Multi-band calibrations of the TRGB absolute magnitude. *The Astronomical Journal*, 156(6):278, nov 2018. doi:10.3847/1538-3881/aaeacb. URL `https://doi.org/10.3847/1538-3881/aaeacb`.

[18] Marek Górski, Bartłomiej Zgirski, Grzegorz Pietrzyński, Wolfgang Gieren, Piotr Wielgórski, Dariusz Graczyk, Rolf-Peter Kudritzki, Bogumił Pilecki, Weronika Narloch, Paulina Karczmarek, Ksenia Suchomska, and Mónica Taormina. Empirical Calibration of the Reddening Maps in the Magellanic Clouds. *The Astrophysical Journal*, 889 (2):179, February 2020. doi:10.3847/1538-4357/ab65ed.

[19] Dariusz Graczyk, Grzegorz Pietrzyński, Ian B. Thompson, Wolfgang Gieren, Bogumił Pilecki, Andrzej Udalski, Igor Soszyński, Zbigniew Kołaczkowski, Rolf-Peter Kudritzki, Fabio Bresolin, Piotr Konorski, Ronald Mennickent, Dante Minniti, Jesper Storm, Nicolas Nardetto, and Paulina Karczmarek. The Araucaria Project: An Accurate Distance to the Late-type Double-lined Eclipsing Binary OGLE SMC113.3 4007 in the Small Magellanic Cloud. *The Astrophysical Journal*, 750(2):144, May 2012. doi:10.1088/0004-637X/750/2/144.

[20] Dariusz Graczyk, Grzegorz Pietrzyński, Ian B. Thompson, Wolfgang Gieren, Bogumił Pilecki, Piotr Konorski, Andrzej Udalski, Igor Soszyński, Sandro Villanova, Marek Górski, Ksenia Suchomska, Paulina Karczmarek, Rolf-Peter Kudritzki, Fabio Bresolin, and Alexandre Gallenne. The Araucaria Project. The Distance to the Small Magellanic Cloud from Late-type Eclipsing Binaries. *The Astrophysical Journal*, 780(1):59, January 2014. doi:10.1088/0004-637X/780/1/59.

[21] Dariusz Graczyk, Grzegorz Pietrzyński, Ian B. Thompson, Wolfgang Gieren, Bogumił Pilecki, Piotr Konorski, Sandro Villanova, Marek Górski, Ksenia Suchomska, Paulina Karczmarek, Kazimierz Stepień, Jesper Storm, Mónica Taormina, Zbigniew Kołaczkowski, Piotr Wielgórski, Weronika Narloch, Bartłomiej Zgirski, Alexandre Gallenne, Jakub Ostrowski, Radosław Smolec, Andrzej Udalski, Igor Soszyński, Pierre Kervella, Nicolas Nardetto, Michał K. Szymański, Łukasz Wyrzykowski, Krzysztof Ulaczyk, Radosław Poleski, Paweł Pietrukowicz, Szymon Kozłowski, Jan Skowron, and Przemysław Mróz. The Late-type Eclipsing Binaries in the Large Magellanic Cloud: Catalog of Fundamental Physical Parameters. *The Astrophysical Journal*, 860(1):1, June 2018. doi:10.3847/1538-4357/aac2bf.

[22] Dariusz Graczyk, Grzegorz Pietrzyński, Ian B. Thompson, Wolfgang Gieren, Bartłomiej Zgirski, Sandro Villanova, Marek Górski, Piotr Wielgórski, Paulina Karczmarek, Weronika Narloch, Bogumił Pilecki, Monica Taormina, Radosław Smolec, Ksenia Suchomska, Alexandre Gallenne, Nicolas Nardetto, Jesper Storm, Rolf-Peter Kudritzki, Mikołaj Kałuszyński, and Wojciech Pych. A Distance Determination to the Small Magellanic Cloud with an Accuracy of Better than Two Percent Based on Late-type Eclipsing Binary Stars. *The Astrophysical Journal*, 904(1):13, November 2020. doi:10.3847/1538-4357/abbb2b.

[23] Jason Harris and Dennis Zaritsky. The Star Formation History of the Large Magellanic Cloud. *The Astronomical Journal*, 138(5):1243–1260, November 2009. doi:10.1088/0004-6256/138/5/1243.

[24] Raoul Haschke, Eva K. Grebel, and Sonia Duffau. New Optical Reddening Maps of the Large and Small Magellanic Clouds. *The Astronomical Journal*, 141(5):158, May 2011. doi:10.1088/0004-6256/141/5/158.

[25] Dylan Hatt, Rachael L. Beaton, Wendy L. Freedman, Barry F. Madore, In-Sung Jang, Taylor J. Hoyt, Myung Gyoon Lee, Andrew J. Monson, Jeffrey A. Rich, Victoria Scowcroft, and Mark Seibert. The Carnegie-Chicago Hubble Program. II. The Distance to IC 1613: The Tip of the Red Giant Branch and RR Lyrae Period-luminosity Relations. *The Astrophysical Journal*, 845(2):146, August 2017. doi:10.3847/1538-4357/aa7f73.

[26] Taylor J. Hoyt, Wendy L. Freedman, Barry F. Madore, Mark Seibert, Rachael L. Beaton, Dylan Hatt, In Sung Jang, Myung Gyoon Lee, Andrew J. Monson, and Jeffrey A. Rich. The Near-infrared Tip of the Red Giant Branch. II. An Absolute Calibration in the Large Magellanic Cloud. *The Astrophysical Journal*, 858(1):12, May 2018. doi:10.3847/1538-4357/aab7ed.

[27] In Sung Jang and Myung Gyoon Lee. The Tip of the Red Giant Branch Distances to Type Ia Supernova Host Galaxies. IV. Color Dependence and Zero-point Calibration. *The Astrophysical Journal*, 835(1):28, January 2017. doi:10.3847/1538-4357/835/1/28.

[28] In Sung Jang and Myung Gyoon Lee. The Tip of the Red Giant Branch Distances to Typa Ia Supernova Host Galaxies. V. NGC 3021, NGC 3370, and NGC 1309 and the Value of the Hubble Constant. *The Astrophysical Journal*, 836(1):74, February 2017. doi:10.3847/1538-4357/836/1/74.

[29] In Sung Jang, Taylor J. Hoyt, Rachael L. Beaton, Wendy L. Freedman, Barry F. Madore, Myung Gyoon Lee, Jillian R. Neeley, Andrew J. Monson, Jeffrey A. Rich, and Mark Seibert. The Carnegie-Chicago Hubble Program. IX. Calibration of the Tip of the Red Giant Branch Method in the Megamaser Host Galaxy, NGC 4258 (M106). *The Astrophysical Journal*, 906(2):125, January 2021. doi:10.3847/1538-4357/abc8e9.

[30] Sungeun Kim, Michael A. Dopita, Lister Staveley-Smith, and Michael S. Bessell. H I Shells in the Large Magellanic Cloud. *The Astronomical Journal*, 118(6):2797–2823, December 1999. doi:10.1086/301116.

[31] L. Lindegren, U. Bastian, M. Biermann, A. Bombrun, A. de Torres, E. Gerlach, R. Geyer, J. Hernández, T. Hilger, D. Hobbs, S. A. Klioner, U. Lammers, P. J. McMillan, M. Ramos-Lerate, H. Steidelmüller, C. A. Stephenson, and F. van Leeuwen. Gaia Early Data Release 3. Parallax bias versus magnitude, colour, and position. *Astronomy and Astrophysics*, 649:A4, May 2021. doi:10.1051/0004-6361/202039653.

[32] L. Lindegren, S. A. Klioner, J. Hernández, A. Bombrun, M. Ramos-Lerate, H. Steidelmüller, U. Bastian, M. Biermann, A. de Torres, E. Gerlach, R. Geyer, T. Hilger, D. Hobbs, U. Lammers, P. J. McMillan, C. A. Stephenson, J. Castañeda, M. Davidson, C. Fabricius, G. Gracia-Abril, J. Portell, N. Rowell, D. Teyssier, F. Torra, S. Bartolomé, M. Clotet, N. Garralda, J. J. González-Vidal, J. Torra, U. Abbas, M. Altmann, E. Anglada Varela, L. Balaguer-Núñez, Z. Balog, C. Barache, U. Becciani, M. Bernet, S. Bertone, L. Bianchi, S. Bouquillon, A. G. A. Brown, B. Bucciarelli, D. Busonero, A. G. Butkevich, R. Buzzi, R. Cancelliere, T. Carlucci, P. Charlot, M. R. L. Cioni, M. Crosta, C. Crowley, E. F. del Peloso, E. del Pozo, R. Drimmel, P. Esquej, A. Fienga, E. Fraile, M. Gai, M. Garcia-Reinaldos, R. Guerra, N. C. Hambly, M. Hauser, K. Janßen, S. Jordan, Z. Kostrzewa-Rutkowska, M. G. Lattanzi, S. Liao, E. Licata, T. A. Lister, W. Löffler, J. M. Marchant, A. Masip, F. Mignard, A. Mints, D. Molina, A. Mora, R. Morbidelli, C. P. Murphy, C. Pagani, P. Panuzzo, X. Peñalosa Esteller, E. Poggio, P. Re Fiorentin, A. Riva, A. Sagristà Sellés, V. Sanchez Gimenez, M. Sarasso, E. Sciacca, H. I. Siddiqui, R. L. Smart, D. Souami, A. Spagna, I. A. Steele, F. Taris, E. Utrilla, W. van Reeven, and A. Vecchiato. Gaia Early Data Release 3. The astrometric solution. *Astronomy and Astrophysics*, 649:A2, May 2021. doi:10.1051/0004-6361/202039709.

[33] Barry F. Madore, Violet Mager, and Wendy L. Freedman. Sharpening the Tip of the Red Giant Branch. *The Astrophysical Journal*, 690(1):389–393, January 2009. doi:10.1088/0004-637X/690/1/389.

[34] Andrew J. Monson, Rachael L. Beaton, Victoria Scowcroft, Wendy L. Freedman, Barry F. Madore, Jeffrey A. Rich, Mark Seibert, Juna A. Kollmeier, and Gisella Clementini. Standard Galactic Field RR Lyrae. I. Optical to Mid-infrared Phased Photometry. *The Astronomical Journal*, 153(3):96, March 2017. doi:10.3847/1538-3881/153/3/96.

[35] T. Muraveva, S. Subramanian, G. Clementini, M. R. L. Cioni, M. Palmer, J. Th. van Loon, M. I. Moretti, R. de Grijs, R. Molinaro, V. Ripepi, M. Marconi, J. Emerson, and V. D. Ivanov. The VMC survey - XXVI. Structure of the Small Magellanic Cloud from RR Lyrae stars. *MNRAS*, 473(3):3131–3146, January 2018. doi:10.1093/mnras/stx2514.

[36] David M. Nataf, Santi Cassisi, Luca Casagrande, Wenlong Yuan, and Adam G. Riess. On the Color-Metallicity Relation of the Red Clump and the Reddening toward the Magellanic Clouds. *The Astrophysical Journal*, 910(2):121, April 2021. doi:10.3847/1538-4357/abe530.

[37] David L. Nidever, Sten Hasselquist, Christian R. Hayes, Keith Hawkins, Joshua Povick, Steven R. Majewski, Verne V. Smith, Borja Anguiano, Guy S. Stringfellow, Jennifer S. Sobeck, Katia Cunha, Timothy C. Beers, Joachim M. Bestenlehner, Roger E. Cohen, D. A. Garcia-Hernandez, Henrik Jönsson, Christian Nitschelm, Matthew Shetrone, Ivan Lacerna, Carlos Allende Prieto, Rachael L. Beaton, Flavia Dell'Agli, José G. Fernández-Trincado, Diane Feuillet, Carme Gallart, Fred R. Hearty, Jon Holtzman, Arturo Manchado, Ricardo R. Muñoz, Robert O'Connell, and Margarita Rosado. The Lazy Giants: APOGEE Abundances Reveal Low Star Formation Efficiencies in the

Magellanic Clouds. *The Astrophysical Journal*, 895(2):88, June 2020. doi:10.3847/1538-4357/ab7305.

[38] S. Nikolaev, A. J. Drake, S. C. Keller, K. H. Cook, N. Dalal, K. Griest, D. L. Welch, and S. M. Kanbur. Geometry of the Large Magellanic Cloud Disk: Results from MACHO and the Two Micron All Sky Survey. *The Astrophysical Journal*, 601(1):260–276, January 2004. doi:10.1086/380439.

[39] Michał Pawlak. Period-luminosity-colour relation for early-type contact binaries. *MNRAS*, 457(4):4323–4329, April 2016. doi:10.1093/mnras/stw269.

[40] S. E. Persson, Barry F. Madore, W. Krzemiński, Wendy L. Freedman, M. Roth, and D. C. Murphy. New Cepheid Period-Luminosity Relations for the Large Magellanic Cloud: 92 Near-Infrared Light Curves. *The Astronomical Journal*, 128(5):2239–2264, November 2004. doi:10.1086/424934.

[41] G. Pietrzyński, D. Graczyk, W. Gieren, I. B. Thompson, B. Pilecki, A. Udalski, I. Soszyński, S. Kozłowski, P. Konorski, K. Suchomska, G. Bono, P. G. Prada Moroni, S. Villanova, N. Nardetto, F. Bresolin, R. P. Kudritzki, J. Storm, A. Gallenne, R. Smolec, D. Minniti, M. Kubiak, M. K. Szymański, R. Poleski, Ł. Wyrzykowski, K. Ulaczyk, P. Pietrukowicz, M. Górski, and P. Karczmarek. An eclipsing-binary distance to the Large Magellanic Cloud accurate to two per cent. *Nature*, 495(7439):76–79, March 2013. doi:10.1038/nature11878.

[42] G. Pietrzyński, D. Graczyk, A. Gallenne, W. Gieren, I. B. Thompson, B. Pilecki, P. Karczmarek, M. Górski, K. Suchomska, M. Taormina, B. Zgirski, P. Wielgórski, Z. Kołaczkowski, P. Konorski, S. Villanova, N. Nardetto, P. Kervella, F. Bresolin, R. P. Kudritzki, J. Storm, R. Smolec, and W. Narloch. A distance to the Large Magellanic Cloud that is precise to one per cent. *Nature*, 567(7747):200–203, March 2019. doi:10.1038/s41586-019-0999-4.

[43] M. J. Reid, D. W. Pesce, and A. G. Riess. An Improved Distance to NGC 4258 and Its Implications for the Hubble Constant. *Astrophysical Journal Letters*, 886(2):L27, December 2019. doi:10.3847/2041-8213/ab552d.

[44] Marina Rejkuba, Laura Greggio, William E. Harris, Gretchen L. H. Harris, and Eric W. Peng. Deep ACS Imaging of the Halo of NGC 5128: Reaching the Horizontal Branch. *The Astrophysical Journal*, 631(1):262–279, September 2005. doi:10.1086/432462.

[45] Adam G. Riess, Lucas M. Macri, Samantha L. Hoffmann, Dan Scolnic, Stefano Casertano, Alexei V. Filippenko, Brad E. Tucker, Mark J. Reid, David O. Jones, Jeffrey M. Silverman, Ryan Chornock, Peter Challis, Wenlong Yuan, Peter J. Brown, and Ryan J. Foley. A 2.4% Determination of the Local Value of the Hubble Constant. *The Astrophysical Journal*, 826(1):56, July 2016. doi:10.3847/0004-637X/826/1/56.

[46] Adam G. Riess, Stefano Casertano, Wenlong Yuan, Lucas M. Macri, and Dan Scolnic. Large Magellanic Cloud Cepheid Standards Provide a 1% Foundation for the Determination of the Hubble Constant and Stronger Evidence for Physics beyond ΛCDM. *The Astrophysical Journal*, 876(1):85, May 2019. doi:10.3847/1538-4357/ab1422.

[47] Vincenzo Ripepi, Maria-Rosa L. Cioni, Maria Ida Moretti, Marcella Marconi, Kenji Bekki, Gisella Clementini, Richard de Grijs, Jim Emerson, Martin A. T. Groenewegen, Valentin D. Ivanov, Roberto Molinaro, Tatiana Muraveva, Joana M. Oliveira, Andrés E. Piatti, Smitha Subramanian, and Jacco Th. van Loon. The VMC survey - XXV. The 3D structure of the Small Magellanic Cloud from Classical Cepheids. *MNRAS*, 472(1): 808–827, November 2017. doi:10.1093/mnras/stx2096.

[48] Luca Rizzi, R. Brent Tully, Dmitry Makarov, Lidia Makarova, Andrew E. Dolphin, Shoko Sakai, and Edward J. Shaya. Tip of the Red Giant Branch Distances. II. Zero-Point Calibration. *The Astrophysical Journal*, 661(2):815–829, June 2007. doi:10.1086/516566.

[49] K. Rohlfs, J. Kreitschmann, B. C. Siegman, and J. V. Feitzinger. A neutral hydrogen line survey of the Large Magellanic Cloud. *Astronomy and Astrophysics*, 137:343–357, August 1984.

[50] Stefano Rubele, Giada Pastorelli, Léo Girardi, Maria-Rosa L. Cioni, Simone Zaggia, Paola Marigo, Kenji Bekki, Alessandro Bressan, Gisella Clementini, Richard de Grijs, Jim Emerson, Martin A. T. Groenewegen, Valentin D. Ivanov, Tatiana Muraveva, Ambra Nanni, Joana M. Oliveira, Vincenzo Ripepi, Ning-Chen Sun, and Jacco Th van Loon. The VMC survey - XXXI: The spatially resolved star formation history of the main body of the Small Magellanic Cloud. *MNRAS*, 478(4):5017–5036, August 2018. doi:10.1093/mnras/sty1279.

[51] Maurizio Salaris and Santi Cassisi. *Evolution of Stars and Stellar Populations*. Wiley, 2005.

[52] Maurizio Salaris and Léo Girardi. Tip of the Red Giant Branch distances to galaxies with composite stellar populations. *MNRAS*, 357(2):669–678, February 2005. doi:10.1111/j.1365-2966.2005.08689.x.

[53] Edward F. Schlafly and Douglas P. Finkbeiner. Measuring Reddening with Sloan Digital Sky Survey Stellar Spectra and Recalibrating SFD. *The Astrophysical Journal*, 737(2): 103, August 2011. doi:10.1088/0004-637X/737/2/103.

[54] David J. Schlegel, Douglas P. Finkbeiner, and Marc Davis. Maps of Dust Infrared Emission for Use in Estimation of Reddening and Cosmic Microwave Background Radiation Foregrounds. *The Astrophysical Journal*, 500(2):525–553, June 1998. doi:10.1086/305772.

[55] D. M. Skowron, J. Skowron, A. Udalski, M. K. Szymański, I. Soszyński, Ł. Wyrzykowski, K. Ulaczyk, R. Poleski, S. Kozłowski, P. Pietrukowicz, P. Mróz, K. Rybicki, P. Iwanek,

M. Wrona, and M. Gromadzki. OGLE-ing the magellanic system: Optical reddening maps of the large and small magellanic clouds from red clump stars. *The Astrophysical Journal Supplement Series*, 252(2):23, feb 2021. doi:10.3847/1538-4365/abcb81. URL `https://doi.org/10.3847/1538-4365/abcb81`.

[56] John Soltis, Stefano Casertano, and Adam G. Riess. The Parallax of ω Centauri Measured from Gaia EDR3 and a Direct, Geometric Calibration of the Tip of the Red Giant Branch and the Hubble Constant. *Astrophysical Journal Letters*, 908(1):L5, February 2021. doi:10.3847/2041-8213/abdbad.

[57] I. Soszyński, A. Udalski, M. K. Szymański, M. Kubiak, G. Pietrzyński, Ł. Wyrzykowski, O. Szewczyk, K. Ulaczyk, and R. Poleski. The Optical Gravitational Lensing Experiment. The OGLE-III Catalog of Variable Stars. IV. Long-Period Variables in the Large Magellanic Cloud. *Acta Astronomica*, 59(3):239–253, September 2009.

[58] I. Soszyński, A. Udalski, M. K. Szymański, M. Kubiak, G. Pietrzyński, Ł. Wyrzykowski, K. Ulaczyk, R. Poleski, S. Kozłowski, and P. Pietrukowicz. The Optical Gravitational Lensing Experiment. The OGLE-III Catalog of Variable Stars. XIII. Long-Period Variables in the Small Magellanic Cloud. *Acta Astronomica*, 61(3):217–230, September 2011.

[59] I. Soszyński, A. Udalski, M. K. Szymański, D. Skowron, G. Pietrzyński, R. Poleski, P. Pietrukowicz, J. Skowron, P. Mróz, S. Kozłowski, Ł. Wyrzykowski, K. Ulaczyk, and M. Pawlak. The OGLE Collection of Variable Stars. Classical Cepheids in the Magellanic System. *Acta Astronomica*, 65(4):297–312, December 2015.

[60] M. K. Szymański, A. Udalski, I. Soszyński, M. Kubiak, G. Pietrzyński, R. Poleski, Ł. Wyrzykowski, and K. Ulaczyk. The Optical Gravitational Lensing Experiment. OGLE-III Photometric Maps of the Galactic Bulge Fields. *Acta Astronomica*, 61(2): 83–102, June 2011.

[61] F. Torra, J. Castañeda, C. Fabricius, L. Lindegren, M. Clotet, J. J. González-Vidal, S. Bartolomé, U. Bastian, M. Bernet, M. Biermann, N. Garralda, A. Gúrpide, U. Lammers, J. Portell, and J. Torra. Gaia Early Data Release 3. Building the Gaia DR3 source list - Cross-match of Gaia observations. *Astronomy and Astrophysics*, 649:A10, May 2021. doi:10.1051/0004-6361/202039637.

[62] A. Udalski. The Optical Gravitational Lensing Experiment. Real Time Data Analysis Systems in the OGLE-III Survey. *Acta Astronomica*, 53:291–305, December 2003.

[63] A. Udalski, M. Kubiak, and M. Szymanski. Optical Gravitational Lensing Experiment. OGLE-2 – the Second Phase of the OGLE Project. *Acta Astronomica*, 47:319–344, July 1997.

[64] A. Udalski, M. Szymanski, M. Kubiak, G. Pietrzynski, I. Soszynski, P. Wozniak, and K. Zebrun. The Optical Gravitational Lensing Experiment. BVI Maps of Dense Stellar

Regions. II. The Large Magellanic Cloud. *Acta Astronomica*, 50:307–335, September 2000.

[65] A. Udalski, I. Soszynski, M. K. Szymanski, M. Kubiak, G. Pietrzynski, L. Wyrzykowski, O. Szewczyk, K. Ulaczyk, and R. Poleski. The Optical Gravitational Lensing Experiment. OGLE-III Photometric Maps of the Large Magellanic Cloud. *Acta Astronomica*, 58:89–102, June 2008.

[66] A. Udalski, M. K. Szymanski, I. Soszynski, and R. Poleski. The Optical Gravitational Lensing Experiment. Final Reductions of the OGLE-III Data. *Acta Astronomica*, 58: 69–87, June 2008.

[67] A. Udalski, M. K. Szymański, and G. Szymański. OGLE-IV: Fourth Phase of the Optical Gravitational Lensing Experiment. *Acta Astronomica*, 65(1):1–38, March 2015.

[68] K. Ulaczyk, M. K. Szymański, A. Udalski, M. Kubiak, G. Pietrzyński, I. Soszyński, Ł. Wyrzykowski, R. Poleski, W. Gieren, A. Walker, and A. Garcia-Varela. Photometric Maps Based on the OGLE-III Shallow Survey in the Large Magellanic Cloud. *Acta Astronomica*, 62(3):247–268, September 2012.

[69] E. Valenti, F. R. Ferraro, and L. Origlia. Red giant branch in near-infrared colour-magnitude diagrams - I. Calibration of photometric indices. *MNRAS*, 351(4):1204–1214, July 2004. doi:10.1111/j.1365-2966.2004.07861.x.

[70] Roeland P. van der Marel and Maria-Rosa L. Cioni. Magellanic Cloud Structure from Near-Infrared Surveys. I. The Viewing Angles of the Large Magellanic Cloud. *The Astronomical Journal*, 122(4):1807–1826, October 2001. doi:10.1086/323099.

[71] Roeland P. van der Marel and Nitya Kallivayalil. Third-epoch Magellanic Cloud Proper Motions. II. The Large Magellanic Cloud Rotation Field in Three Dimensions. *The Astrophysical Journal*, 781(2):121, February 2014. doi:10.1088/0004-637X/781/2/121.

[72] Roeland P. van der Marel, David R. Alves, Eduardo Hardy, and Nicholas B. Suntzeff. New Understanding of Large Magellanic Cloud Structure, Dynamics, and Orbit from Carbon Star Kinematics. *The Astronomical Journal*, 124(5):2639–2663, November 2002. doi:10.1086/343775.

[73] Martin D. Weinberg and Sergei Nikolaev. Structure of the Large Magellanic Cloud from 2MASS. *The Astrophysical Journal*, 548(2):712–726, February 2001. doi:10.1086/319001.

[74] Wenlong Yuan, Adam G. Riess, Lucas M. Macri, Stefano Casertano, and Daniel M. Scolnic. Consistent calibration of the tip of the red giant branch in the large magellanic cloud on the hubble space telescope photometric system and a redetermination of the hubble constant. *The Astrophysical Journal*, 886(1):61, nov 2019. doi:10.3847/1538-4357/ab4bc9. URL `https://doi.org/10.3847/1538-4357/ab4bc9`.